Analysis and Simulation of 3D Scattering due to Heterogeneous Crustal Structure and Surface Topography on Regional Phases; Magnitude and Discrimination

Arben Pitarka
Donald V. Helmberger

URS Group, Inc.
566 El Dorado Street, 2nd Floor
Pasadena CA 91101

Final Report

7 July 2009

AIR FORCE RESEARCH LABORATORY
Space Vehicles Directorate
29 Randolph Rd
AIR FORCE MATERIEL COMMAND
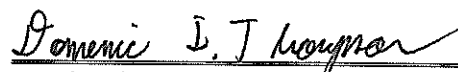**HANSCOM AFB, MA 01731-3010**

NOTICES

Using Government drawings, specifications, or other data included in this document for any purpose other than Government procurement does not in any way obligate the U.S. Government. The fact that the Government formulated or supplied the drawings, specifications, or other data does not license the holder or any other person or corporation; or convey any rights or permission to manufacture, use, or sell any patented invention that may relate to them.

This report was cleared for public release and is available to the general public, including foreign nationals. Qualified requestors may obtain copies of this report from the Defense Technical Information Center (DTIC) (http://www.dtic.mil). All others should apply to the National Technical Information Service.

AFRL-RV-HA-TR-2009-1058 HAS BEEN REVIEWED AND IS APPROVED FOR PUBLICATION IN ACCORDANCE WITH ASSIGNED DISTRIBUTION STATEMENT.

ROBERT J. RAISTRICK
Contract Manager

Domenic Thompson, Maj, USAF, Acting Chief
Battlespace Surveillance Innovation Center

This report is published in the interest of scientific and technical information exchange, and its publication does not constitute the Government's approval or disapproval of its ideas or findings.

REPORT DOCUMENTATION PAGE

1. REPORT DATE *(DD-MM-YYYY)* 07-07-2009	**2. REPORT TYPE** Final Report	**3. DATES COVERED** *(From - To)* 01-29-2007 to 06-30-2009

4. TITLE AND SUBTITLE

Analysis and Simulation of 3D Scattering due to Heterogeneous Crustal Structure and

Surface Topography on Regional Phases; Magnitude and Discrimination

5a. CONTRACT NUMBER
FA8718-07-C-0003

5b. GRANT NUMBER

5c. PROGRAM ELEMENT NUMBER
62601F

6. AUTHOR(S)
Arben Pitarka and Donald V. Helmberger[1]

5d. PROJECT NUMBER
1010

5e. TASK NUMBER
SM

5f. WORK UNIT NUMBER
A1

7. PERFORMING ORGANIZATION NAME(S) AND ADDRESS(ES)

URS Group, Inc.
566 El Dorado Street, 2nd Floor
Pasadena CA 91101

8. PERFORMING ORGANIZATION REPORT NUMBER

9. SPONSORING / MONITORING AGENCY NAME(S) AND ADDRESS(ES)

Air Force Research Laboratory
29 Randolph Rd.
Hanscom AFB, MA 01731-3010

10. SPONSOR/MONITOR'S ACRONYM(S)
AFRL/RVBYE

11. SPONSOR/MONITOR'S REPORT NUMBER(S)
AFRL-RV-HA-TR-2009-1058

12. DISTRIBUTION / AVAILABILITY STATEMENT

Approved for Public Release; Distribution Unlimited.

13. SUPPLEMENTARY NOTES
[1]California Institute of Technology, 1200 East California Blvd., Pasadena CA 91125

14. ABSTRACT
This report concentrates on generating physical explanation for commonly used discriminants. It begins with a brief review of broadband observations from earthquakes and an explosion occurring in North Korea. By comparing detailed earthquake modeling results, we confirm the existence of radiation pattern for body wave arrival onsets to high-frequency, > 8 Hz. We also addressed the coda-levels for all three components and demonstrate that the (P/S) spectral levels provide a useful discriminant, especially at large distances at frequencies > 2 Hz. To simulate these features, we performed anelastic 3D finite-difference calculations on highly heterogeneous media for a range of source depths, receiver distances, and source-types. In this first stage, we investigated the effects of small-scale crustal heterogeneities including fault-damaged zones. In the second stage, we investigated the effects of surface topography including mini-basins combined with crustal heterogeneities. Our numerical experiments show that wave-path scattering is a major contributor to S and Lg coda from shallow explosions and depends on source depth. P/Lg ratios estimated at different frequencies indicate that it is indeed an excellent discriminant at high frequency. However, at frequencies below 2 Hz, explosions and earthquakes look the same for realistic crustal models containing shallow mini-basins. A second possible discriminant is the ratio P (high frequency) / P (low frequency) or P (2 to 4 Hz) / P (.1 to 2 Hz) that works particularly well at small distances. This appears to be caused by the effect of pP on the shallow explosion. A product discriminant of [P (hf) / P (lf) · (P/S)] should work best according to our simulations.

15. SUBJECT TERMS
3D scattering, Surface topography, Seismic wave propagation

16. SECURITY CLASSIFICATION OF:			**17. LIMITATION OF ABSTRACT**	**18. NUMBER OF PAGES**	**19a. NAME OF RESPONSIBLE PERSON** Robert Raistrick
a. REPORT UNC	**b. ABSTRACT** UNC	**c. THIS PAGE** UNC	SAR	59	**19b. TELEPHONE NUMBER** *(include area code)*

Table of Contents

Figures

1. SUMMARY

This report concentrates on generating physical explanation for commonly used discriminants. It begins with a brief review of broadband observations from earthquakes and an explosion occurring in North Korea. By comparing detailed earthquake modeling results, we confirm the existence of radiation pattern for body wave arrival onsets to high-frequency, > 8 Hz. We also addressed the coda-levels for all three components and demonstrate that the (P/S) spectral levels provide a useful discriminant, especially at large distances at frequencies > 2 Hz. To simulate these features, we performed anelastic 3D finite-difference calculations on highly heterogeneous media for a range of source depths, receiver distances, and source-types. In this first stage, we investigated the effects of small-scale crustal heterogeneities including fault-damaged zones. In the second stage, we investigated the effects of surface topography including mini-basins combined with crustal heterogeneities. Our numerical experiments show that wave-path scattering is a major contributor to S and Lg coda from shallow explosions and depends on source depth. P/Lg ratios estimated at different frequencies indicate that it is indeed an excellent discriminant at high frequency. However, at frequencies below 2 Hz, explosions and earthquakes look the same for realistic crustal models containing shallow mini-basins. A second possible discriminant is the ratio P (high frequency) / P (low frequency) or P (2 to 4 Hz) / P (.1 to 2 Hz) that works particularly well at small distances. This appears to be caused by the effect of pP on the shallow explosion. A product discriminant of [P (hf) / P (lf) · (P/S)] should work best according to our simulations.

2. INTRODUCTION

The objective of this study is to analyze and evaluate the effect of scattering on amplitude and frequency content of Pg and Lg waves due to small-scale crustal heterogeneities and surface topography through 3D finite-difference simulations and modeling of recorded waveform data. This objective is relevant to the urgent need for accurate measurements of Lg wave amplitude and frequency content for magnitude and yield discrimination.

The research is focused on the following topics:

1. Influence of scattering due to complex structure and surface topography on the variability observed in amplitude estimates of regional phases. We analyzed simulation results of regional wave propagation scattering, obtained with efficient three-dimensional (3D) finite-difference computer programs that can also treat surface topography, including mini-basins.
2. Influence of scattering effects due to rough topography near the source and station on the amplitude of observed regional phases, involving explosion source.
3. Implication of wave scattering effects in P/S discriminants between earthquakes and explosions.

The main purpose of the study is basic understanding of scattering and its effects through step-by-step numerical experiments and waveform modeling, with the goal of providing useful insights into ongoing research for development of simple empirical models of scattering that can be used in reducing the scatter in measures of Lg and coda wave magnitude observed in some regions. Coda waves are created by wave scattering caused by heterogeneous crustal structure and surface topography. They provide precise but relative measurements of seismic amplitude, therefore scalar moments are needed to adjust the measurements to absolute units (e.g., Mayeda *et al.*, 2005).

In an investigation of regional coda waves Phillips *et al.* (2001) found that strong laterally varying effects of underground structure correlate well with known Lg path effects in central Asia as shown in Phillips *et al.* (2000). However the amplitude of Lg phase and coda waves strongly depends on small scale structural variation in the upper crust which contributes to phase conversions and local wave focusing. Propagation of Lg waves is also affected by surface topography (Zhang, T. and T. Lay, 1994) including mountain ranges (e.g., Ruzaikian *et al.*, 1977; Ni and Barazangi, 1983) and surface topography in the source region. Because of the lack of robust numerical techniques this is an area that has received little attention. Some success has been attained in the theoretical explanation of the blockage of regional phases by topography. However Campilllo *et al.* (1992) were unable to explain the sharp decrease in amplitude for Lg along a path across the Alps. In this study, we have investigated the effects of scattering due to small-scale heterogeneities in the crust, and seismic scattering due to regional surface topography in relation to source type, source depth and surface geology.

Another important problem in seismic source discrimination is the generation of S waves from explosion sources. Regional recordings of underground nuclear tests show S phases, particularly Lg, on all three components. Several hypotheses suggest that part of the S waves are generated at the source region due to complex interaction between the compressional waves and material properties including cavities, cracks and topography around the source, and that other parts are generated by seismic scattering that causes wave type conversion. Wave type conversion produces energy on components where there would be none in a plane-layered medium. Patton and Taylor (1995) have suggested Rg to S (Lg) scattering. Scattering of Rg to body waves, including S waves, by topography (Bullitt and Toksoz, 1985; Jih, 1994) and by near surface heterogeneity has been demonstrated by some numerical models. For example using simple 2D and 3D finite difference calculations, McLaughlin *et al.* (1993), and Stead and Helmberger (1988) have shown that azimuthal variation of the wavefield can vary greatly depending on the exact location of the explosion with reference to the rock free surface. Calculations by Stevens *et al.* (1993) also showed that the radiation from an explosion in a mountain was very sensitive to elevation above the surface surrounding the mountain. More complex free-surface diffraction and reflection effects are expected from small earthquakes which have a complex source radiation pattern.

Building upon experience gained over many years and recent numerical techniques for modeling the source, surface topography and wave propagation (e.g., Xie *et al.*, 2005; Toksoz *et al.*, 2005; Myers *et al.*, 2005;) we developed 3D velocity models to investigate

the generation of S waves from explosion sources and implication of wave scattering in source discrimination. An essential feature of the regional models and their analyses is the localization of the structures causing the fluctuations to the lithosphere immediately below the array or below and above the earthquake or explosion source. Fluctuations of amplitude affect the accuracy of magnitude determination, and hence yield estimation. The fluctuations are reflected in the scattering of Lg magnitudes and their stability. Here we examine the relative contributions of wave-field scattering and absorption effects on different frequency bands of Lg and coda waves due to localized small-scale bodies embedded in a crustal velocity model, randomly distributed near the source and away from the source.

2.1 Observed Regional Seismic Wave Propagation Scattering

We analyzed scattering effects on recorded regional seismograms from earthquakes in South Korea. In particular we have analyzed envelopes of broad-band velocity seismograms at different frequency bands, recorded at stations near nodal planes. The coda of P and S waves near nodal planes are both direct products of wave scattering. Therefore the comparison of the three components of motion at such stations could give useful information about the size of random structural complexities responsible for the observed coda waves. This information is crucial in guiding the development of our new scheme that was used to model random spatial perturbations of the velocity.

We investigated the amplitude variation of the ground velocity envelope as a function of frequency from the Mw4.5 earthquake in South Korea, Figure 1. We used broad-band recordings for most of these stations with a few near-in observations included, at stations CHC, CHJ, ULJ, and SES. The station and the earthquake locations are displayed. The earthquake was located at a depth of 11 km. Its focal mechanism (strike=209°, dip=90°, rake=180°) was determined using a cut and paste (CAP) inversion technique that is based on different weights for relatively high frequency waveform modeling of Pnl and relatively long period surface waves (Tan *et al*., 2006). Pnl and surface waves are also allowed to shift in time to take into account of uncertainties in velocity structure. Joint inversion of Pnl and surface waves provides better constraints on focal depth as well as source mechanisms. The pure strike-slip mechanism of the earthquake and its recording at stations near the P wave nodal planes are ideal for analyzing regional scattered waves. Figure 2 shows the amplitude variation of the ground velocity envelope as a function of frequency at four stations. Stations CHJ and CHC are close to P-wave nodal planes. At these stations the tangential component of motion is much higher than the two others. The epicentral distance of the considered stations varies from 69 km at CHJ to 214 km at SES. Several general observations relevant to the wave scattering can be made.

First, the relatively large amplitude of the direct P wave on the vertical and radial components observed at the non-nodal stations ULJ and SES remains significant even at frequencies higher then 8Hz. This indicates that the radiation pattern of the P waves is effective even at such high frequencies. In contrast, the P wave scattering, expressed as the relative increase of amplitude of the P wave and its coda in the tangential component of motion at P-wave nodal stations, becomes significant at frequencies higher than 4 Hz. Note the relatively large amplitude of P coda waves on the tangential component at such

3

frequencies. This indicates that P to S-wave conversions are significant at high frequencies. As it will be shown later, scattering effects due to small-scale perturbations in the shallow crust cause similar increase in amplitude of high frequency P-wave coda in all three components. Amplitude changes of P waves and their coda as a function of frequency could be very helpful in constraining the basic parameters of scattering models.

Second, because of their shorter wavelength S waves are more susceptible to wave propagation scattering effects. As shown in Figure 2, for such waves the amplitude difference between the three components that is controlled by the source radiation pattern is observed only at frequencies lower than 2 Hz. At frequencies higher then 4Hz, and independently of the epicentral distance, the amplitude of S wave coda is the same for all three components. This suggests that at high frequencies the amplitude of S wave coda does not follow the source radiation pattern. This example shows that at high frequencies the S wave radiation pattern is mainly controlled by wave scattering in the crust. This very robust feature of S coda waves could be used to derive stable estimates of source parameters.

We also observed that the ratio between Pn and Pg seems to be stable over different frequencies. For strike slip events such as the 070120 Korean earthquake, Pn should be much smaller than Pg because of its steeper takeoff angle. But for explosions, Pn and Pg seem to have similar amplitudes (Kim and Richards, 2007). For the Korean earthquake, Pn is indeed much weaker than Pg for all the frequency bands, suggesting that the ratio between Pn and Pg can be used to constrain source mechanisms event at high frequencies, and should be very useful for discrimination purposes. Based on this investigation we derived the following conclusion:

1. Source Radiation pattern of P waves starts to break down only at above 8Hz.

2. Significant increase in amplitude of P coda waves in the tangential component above 4 Hz due to P-S conversions.

3. S waves are more susceptible to wave propagation scattering. The radiation pattern effect of S waves is largely distorted at frequencies above 2 Hz. At these frequencies the amplitude of all three components becomes the same.

2.2 Observed Scattering Effects on Waveforms from Earthquakes and Explosions

The origin of the high frequency scattering affecting mainly the P, Rg and Lg coda waves (above 1Hz) could be due to either deep or shallow crustal structure complexities along the wave path or in the source region (e.g., Dainty 1996; Wu *et al*., 2000, He *et al*., 2008). Several studies have shown that the Lg wave scattering is related to small-scale structural heterogeneities. Other causes of scattering could also be large-scale structural complexities such as crustal thinning or multipathing in the crust and large basins (e.g., Ni and Barazangi, 1983; Phillips *et al*., 2000).

4

We investigated the effect of wave scattering on broad-band waveforms in connection with the source depth and distance. We analyzed smoothed waveform envelopes from the North Korean explosion and the 020416 M4.5 earthquake in North Korea recorded at close and intermediate distances, about 100 km for STATION1 and 400 km for MDJ, respectively. The earthquake, explosion and stations location are shown in Figure 3. STATION 1 which is not shown in this figure is located south west of MDJ. The epicentral distance between the earthquake and explosion is about 60 km. Knowing that the geological structures along the azimuthal direction of the two stations are very different it is expected that the wave scattering will have different effects on the corresponding waveforms. However we want to see whether or not such effects are also dependent on distance, source depth and type of waves.

Figure 4a shows smoothed envelopes of broad-band velocity seismograms from the 020416 earthquake recorded at station MDJ and STATION 1. The envelopes are calculated at the frequency bands of 0.8-2 Hz and 4-8 Hz. An interesting feature of the envelopes is the decay rate of P coda waves. At STATION1, which is closer to the source, the decay rate of P coda wave amplitude is much higher than that at MDJ. P to S wave conversions due to structural complexities and the complex free surface geometry provide more energy to P coda waves. The recording at MDJ shows such scattering effect increases with distance. Also in contrast with MDJ, at STATION1 the amplitude ratio between P and S waves does not change with frequency. This tells us that wave scattering at short distances have similar effects on direct P and S waves. These observations suggest that in this particular region the wave propagation scattering is azimuthally dependent. Scattering is stronger on the S wave then the P wave and along the path to MDJ which is also the longest. As a consequence the S/P ratio at MDJ is strongly reduced at high frequencies in all three components.

It is interesting to see whether such effects depend on the source type. We performed the same analyses to the explosion waveforms at MDJ and STATION1. Figure 4b shows smoothed waveform envelopes for the 061009 North Korean explosion calculated at MDJ and STATION1. The explosion waveforms are rich in S wave energy, in particular at STATION1 which is closer to the source. The difference in wave scattering between the two stations observed during the earthquake remains visible even for the explosion source. The similarities between the explosion and earthquake suggests that the observed difference in scattering effects between the two stations is rather shallow and not strictly related to the source region.

The comparison of waveform envelopes between the earthquake and explosion is shown in Figure 4c. Note that along the short wave path to STATION1, with low wave path scattering, P/S coda waves amplitude ratios for the earthquake and explosion are very similar. In contrast along the wave-path to MDJ which is longer and with strong wave scattering the P/S ratios between the earthquake and explosion are very different. P/S ratio for the explosion at MDJ is much larger. These observations suggest that at large epicentral distances the cumulative effect of wave scattering on P/S coda wave ratio is enhanced. Therefore at large distances the P/S coda wave ratio could be a good discriminant between earthquakes and explosions. This observation is very well reproduced by our subsequent simulations of 3D wave scattering.

3. Fault Zone Wave Scattering: Big Bear, California Earthquake Sequence

The Joint Verification Experiment indicated that a magnitude (m_b) bias (δm_b) exists between the Semipalatinsk Test Site (STS) in the former Soviet Union (FSU) and the Nevada Test Site (NTS) in the United States. Generally δm_b is attributed to differential attenuation in the upper mantle beneath the two test sites. This assumption results in rather large estimates of yield for large m_b tunnel shots at Novaya Zemlya. A re-examination of the US testing experiments suggests that δm_b can partly be explained by anomalous NTS (Pahute) source characteristics. This variation is probably due to variations in source conditions. Studies that combine analyses of regional and teleseismic data from NTS nuclear explosions and local earthquakes and 3D wave propagation modeling can provide valuable information on near-source shallow structure affects on depth phases and near-source wave scattering. Such data is extremely useful in comparative studies of the target and master events.

Near-source wave scattering has a great implication in shaping the source energy radiation at local and teleseismic distances. It also affects the amplitude of depth phases. Due to limited knowledge of small-scale crustal heterogeneities and insufficient near-source recorded waveform data, source region wave scattering is often neglected in studies of focal mechanism and magnitude estimates, in particular for events located in tectonically complex regions. Two types of source region scattering are relevant to our study which is aimed at investigating empirical source discrimination techniques using coda waves. The first is fault zone wave scattering, a well known phenomena that have been the focus of many recent studies. The second is scattering due to local topography and microbasins near shallow seismic sources.

Several studies have shown strong evidence of fault zone wave scattering described as fault zone trapped waves. Most of them are focused on near-fault ground motion characteristics. By using very high quality date Tan and Helmberger (2009) have been able to demonstrate significant effects of fault zone complexities on rupture characteristics. Their waveform crosscorrelation analysis could be used as diagnostication tools for detecting fault zone effects on P and S coda waves at regional distances. Here we briefly describe the essence of their study and its implication to understanding the fault zone scattering.

Tan and Helmberger (2006) analyzed broad-band waveform data to infer focal mechanism, rupture directivity, kinematic rupture, and stress drop parameters for a large number of earthquakes from the 2003 Big bear earthquake sequence (Figure 5). Their technique uses small events as Empirical Green's functions to calculate Relative Source Time Functions (RSTF). RSTF are then used to derive the rupture directivity. Figure 6 shows inferred rupture direction for selected events. For these events the rupture planes have complex orientation indicating complex faulting. In particular, ruptures propagate in all directions, with wide-ranged rupture speeds. For example, although they are closely located, the neighboring events, 13935996 (Event 1) and 13936596 (Event 5), rupture on conjugate fault planes, suggesting cross-over faults at depth. Besides, the

events that are both located on the main shock fault plane, e.g., 13937492 (Event 7) and 13935996 (Event 1) rupture in completely opposite directions, which indicates heterogeneity of the fault plane or complexity of the fault zone.

The Big Bear earthquake sequence shows a clear relationship between the relative location of small earthquakes with respect to mainshock, and their source characteristics. Small events located near the main event (NF) have relatively low stress drop and relatively large rupture velocity and fault length compared to more distant cross-fault events (DF) to the north, Figure 7, Tan *et al*. (2006). In addition, the NF events display more complexities between the P-wave-train and S-wave-train. Many of these events have relatively complex S-waves compared to the DF events. The P-waves seem relatively stable since they were able predict the differences based on directivity estimates and fault parameters. However, many of the S-waves are observationally more complex when we applied waveform intercorrelation between an event located inside the fault zone and an event located outside the fault zoned (Figure 8). As shown in this figure the quality of the intercorrelation at station DPP for event 1396326 and event 13937600 is different for P waves and S waves. This suggests that these complexities are caused by wave propagation scattering in the fault damage zone where the sources are located. The small scale heterogeneities affect the S waves more than the P waves which have longer wavelengths. We argue that this feature is caused by fault-zone damage where energy is locally trapped in the slow leaky waveguide and then re-radiated from the lateral edges of the fault zone. In a subsequent section we will show results of our modeling of fault zone wave scattering. Our 3D numerical simulation demonstrates the implication of fault zone damage on observed waveform scattering of P and S waves.

4. Simulation of 3D Wave Scattering Using Finite-Difference Method

Early studies on attenuation demonstrated that velocity fluctuations with alternating high and low velocity layers, similar to those found in well logs, are most effective in removing high frequencies from the earliest portion of the transmitted wave train (e.g., Saikia, 2006). We used velocity fluctuations in 3D media to duplicate this feature commonly observed geologically in stratigraphy as alternating layers of shale and sandstones in sedimentary layers or alternating layers of gabbro and granite in bedrock.

The influence of crustal random heterogeneities of all scales and surface topography are shown to be very important factors influencing the scattered waves observed as coda waves. While analyses of recorded seismograms can reveal the degree of complexities in the crust and the effect of small scale and large- scale perturbation on different wave phases, the numerical experiments can be used for isolating effects caused by the wave path, seismic source, and local structures. They can also be used to verify hypothesis that are at the foundation of several discrimination methodologies and complement studies of waveform analyses in regions with sparse station coverage.

Recent studies of wave propagation based on three-dimensional finite-difference methods (3D-FDM) have contributed to a better understanding of the heterogeneous path and source process (Myers *et al*., 2003; Pitarka *et al*., 1998, Graves *et al*.,1998; Graves and Pitarka 2004; Frankel and Vidale,1992). A common feature of the 3D-FDM

techniques applied in most of these studies is the use of the uniform-grid formulation with constant grid spacing, which requires relatively large computer memory. Due to computational limitations, these studies are restricted to long periods (usually longer than 1s), and use relatively high values for the shear velocity of the near-surface sediments. 3D-FDM techniques capable of extending these calculations to shorter period seismograms at large distances without additional computer memory are essential to understand the influence of the propagation model in the regions of CTBT interest, where geologic features are complex. A significant improvement in the 3D finite-difference technique was made by the application of the finite-difference operators on 3D grids with variable spacing (Pitarka 1999). This, combined with parallel processing, enables the modeling of wave propagation at high frequencies using realistic crustal velocity models. Our 3D-FDM computer code solves the stress-velocity equations in a heterogeneous medium using staggered grids based on such technique. The code can also treat heterogeneous structure with surface topography and rupture dynamics as well (Pitarka and Irikura, 1996, and Pitarka and Dalguer, 2003). The technique is an excellent approach to modeling complex wave propagation in regional settings.

In this study we apply a 3D staggered grid finite difference technique and a grid with variable spacing (Pitarka, 1999) to simulate the effect of surface topography and shallow crustal heterogeneity on wave propagation scattering on both isotropic explosion and earthquake sources. Our finite difference code solves the stress-velocity wave equations in a heterogeneous medium using staggered grids. Anelastic attenuation is implemented efficiently using relaxation times between stress and strain based on the viscoelastic modulus representation (e.g., Day and Bradley [2001]; Graves and Day [2003]). The technique for generating the 3D velocity model on a regular grid with variable spacing allows for inclusion of small-scale complexities and surface topography as well. The technique we use to model free surface topography is an extension of the formalism that we have applied to modeling wave propagation in media with curved free surface (Pitarka and Irikura, 1996). The performance of our free-surface boundary condition technique at handling Lg coda waves for flat free surface and very long distances was compared with that of the FK method of Saikia (1994) for a shallow source. Also the technique has been validated against other standard and accurate techniques for modeling surface topography such as 2D-Boundary Element Method (BEM) and the 2D-Discrete Wavenumber-Boundary Integral Equation method of Takenaka *et al*. (1996).

4.1 Parameterization of Scattering Model

The wave scattering effects in our 3D simulations are modeled by random perturbations of the velocity. The perturbations expressed in percentage of unperturbed shear-wave velocity are spatially correlated using a correlation length. Results of sensitivity analyses with different velocity perturbations and correlation lengths, not shown here, confirm the importance of these parameters in producing realistic wave path scattering on a broad frequency range. One way of deriving realistic scattering model parameters is to simulate observed broad-band waveforms from small and moderate regional earthquakes using random perturbations of well calibrated velocity models. The objective of such modeling is to derive scattering parameterization of the velocity model by reproducing the gradual disappearance of the observed radiation pattern of P and S

waves with increasing frequency. This is known to be caused by near-source and wave-path scattering. The use of both P and S waves as well as their respective codas decay provide excellent empirical constraints on deriving realistic random velocity perturbations with correct correlation lengths.

In our scheme for generating velocity perturbation of the 3D velocity model a random number generator is used to assign a velocity perturbation to each point in the 3D grid. Originally we had planed to use 3D random media following the three types used by Frankel and Clayton (1986). The correlation functions for the Von Karman, exponential, and Gaussian functions represent these types of media statistically. The Fourier transforms of the correlation functions represent the power spectrum density of the medium fluctuations. Figure 9 shows three-dimensional dimensional media with random velocity variations based on exponential and von Karman functions.

In 2D the Gaussian and exponential functions require a small computer memory even for large models. However 2D Fourier transforms are computationally expensive, especially for regional velocity models. An alternative method that yields random perturbations of the velocity model with similar statistical properties is the technique we have applied in this study. The spatial perturbation of velocity in our 3D random model is expressed in percentage of unperturbed shear modulus μ. The random perturbations are inter-correlated using a spatial correlation length D. The perturbed shear modulus μ^{*} at e given grid node 'k' is calculated using the following equation:

$$\mu_k^* = \mu_k (1 + 0.10 f_k)$$

where :

$$f_k = \frac{\sum_1^N \omega_i * rand_i}{W_k} \qquad W_k = \sum_1^N \omega_i \qquad \omega_i = \exp(-\frac{d_i^2}{D^2})$$

- $rand_i$: a spatial distribution of real random numbers ranging between -1 and 1.
- d_i :   distance between the given node 'k' and adjacent nodes
         located within an ellipsoid centered at node 'k' with horizontal
         long axis D and short axis D/2.
- D :   correlation length. D = 1.5 km.

The wave scattering effects in our 3D simulations are modeled by random perturbations of the velocity. The perturbations expressed in percentage of unperturbated shear-wave velocity are inter-correlated using a spatial correlation length. The scattering parameters such as the amount of perturbation (in this case 10%) and its correlation length were derived during the previous phase of this study. Velocity perturbation of up to 10% with a correlation length of 1.5 km was found to correctly reproduce the observed P and S coda waves decay, and the disappearance of their corresponding frequency-dependent radiation pattern. This simple scheme is far less time consuming than other scheme which use 3D Fourier transforms. A similar approach is used to generate the

surface topography. A typical velocity model with irregular surface topography and random velocity perturbations used in this study is illustrated in Figure 10. In this model the maximum elevation is 1400m, and the correlation length of the topographical random variations is 3 km.

5. Effect of Seismic Source Depth on Simulated Wave Scattering

Extensive analyses of short-period teleseismic P-waves from NTS explosions performed by Lay and Zhang (1992) in the time domain and Gupta and McLaughlin (1989) in the frequency domain reveal that the deeper events are simpler than the shallower ones. They both suggest that this could be caused by the increased scattering of shallow complex structure as proposed by McLaughlin, (1986). Some detailed 2D modeling studies for Yucca Flats events support this interpretation (e.g., Stead and Helmberger, 1988). Yucca Flats has been heavily used with over 40 shots of magnitudes greater than 5 and a large number of other smaller ones.

We have examined combined effects of wave propagation scattering due to complexities in the shallow crust and surface topography in relation with the source depth. These effects were investigated by calculating synthetic seismograms for two double couple point sources located at a depth of 2km and 10 km, respectively. The velocity model used in the simulations is shown in Figure 10. The small-scale variations of the velocity are randomly distributed along the top 5km of the crust. The velocity fluctuations are in the range of 2-10% and their correlation length is 3 km. In addition to small-scale fluctuations our velocity model includes several microbasins with sizes varying between 20-40 km and depth up to 3.5 km. The elevation of surface topography varies between 0 and 1400m. The correlation length of topography random variations is 1.5 km. The selected minimum grid spacing of 200 m ensures accurate wave propagation modeling up to 1.8 Hz. The ground motion velocity was computed on a linear array of stations located on the free surface. The stations spacing is 4 km, and the maximum epicentral distance is 130 km. As shown in Figure 10 several stations are located in basins.

We investigated the relative contribution of wave-field scattering on different frequency bands. The comparison between the two scenarios is shown in Figure 11. Figure 11 shows the vertical component of synthetic velocity time histories band-pass filtered at two frequency bands, 0-1Hz and 1-1.8 Hz. At low frequencies (< 1Hz) the waveforms are dominated by the S wave and surface waves for both the deep and shallow sources. However the amplitude and duration of the surface waves are very different between the two sources. As a result of a cumulative scattering effect and probably better trapping in the shallow crust of converted waves at the free surface the shallow source generate coda waves with longer duration. This feature is more distinctive at basin sites (blue traces in Figure 11). However, at higher frequencies (> 1Hz) these differences are insignificant. This is clearly seen in Figure 12 where we compare the slope of S wave coda in smoothed envelopes of waveforms calculated at stations S16 and S26. The difference in the envelope slope for scattered S waves between deep and shallow sources is noticeable only at low frequencies (<1 Hz). At high frequencies the slope remains unchanged at both selected sites suggesting a stable shallow scattering effect. This result

suggests that in relation with the source depth high frequency scattering is more stable than the low frequency scattering. Therefore the slope of the smoothed envelope of the low frequency part of the signal could be used to discriminate between shallow and deep events.

6. Effect of Source Type: Comparison of Earthquakes and Explosions

Finally, using 3D modeling we will investigate the effect of scattering on Lg and coda wave propagation due to topography above the source as a function of frequency band and source depth. For this experiment we will generate regional and far-regional seismograms for explosion sources and examine physical conditions related to scattering that can excite S waves. (Stead, 1989; Saikia *et al*., 2001, Stevens *et al*., 2003; Rodgers and Tromp, 2005). The point source model will also include spall (e.g., Day and McLaughlin,1991; Patton and Taylor, 1995).

Aiming at understanding scattering effects in relation with source type we performed simulations for an isotropic explosion point source located at a depth of 400 m, and an earthquake double-couple point source located at a depth of 2 km. The source location and station locations are shown in Figure 10. Since we are investigating mechanisms of S wave generation, not related to the source, in our simulations we used an isotropic explosion point source model. The source time function for both earthquake and explosion has a flat spectrum in the considered frequency range. The source time function for the earthquake is a "bell-shape" and for the explosion is a modified Haskell type.

Figure 13 shows the comparison of the vertical component of velocity seismograms calculated at a linear array of stations crossing two basins (see Figure 10). We observed the relative amplitude of P and S coda waves in the frequency ranges of 0.1-1.0 Hz and 1.0-1.8 Hz.

Both sources generate S coda and Rg waves that are energetic even at short distances. The effects of shallow heterogeneities and surface topography on wave type conversions such as P to S and S to P as well Rg surface waves are very impressive, especially for the explosion source. Our numerical experiment clearly shows that wave-path scattering alone caused by rough topography and crustal heterogeneities can produce S coda waves with significant energy even for the explosion sources. It is important to note that P coda waves become more energetic a longer distances. The Rg wave dominates the later phases in explosion seismograms. Their amplitude is larger than that of the direct P wave. However at high frequencies (above 1Hz) the Rg waves quickly attenuate with distance. Because of the Rg to Lg conversions caused by the surface topography the amplitude of Rg waves at longer distances is comparable with that of the P waves.

Our simulation suggests that the amplitude ratio between P and Rg coda waves is still higher for the explosion source at high frequencies. This important characteristic is used in developing a stable discrimination technique. Our simulations clearly show that because S coda waves have shorter wavelength their amplitude diminishes faster than that of P coda waves at long distances. This means that in general P/S type discriminants may

work better for longer distances. This result is in agreement with similar observations made when we compared the North Korean explosion and a nearby earthquake at short and regional distances, as displayed in Figure 4c.

As demonstrated by the comparison of smoothed envelopes of waveforms calculated at two selected stations (Figure 14) P coda waves from the explosion have relatively large amplitudes compared to P coda waves from the earthquake. The cumulative effect of scattering caused by the surface topography and spatial structural heterogeneities contribute to generation of P coda waves through P/S and S/P conversions. Contrary to low frequencies, at high frequencies the difference of P/Rg ratio between the explosion and the earthquake source is significant. Our simulations demonstrate that the P/Rg wave ratio could be a good discriminant between the earthquake and explosion sources. However, as we will later show, the performance of this discriminant becomes poor when the earthquake is not very shallow and the explosion is not located near a complex boundary (e.g., Saikia, 1992).

7. Effects of Explosion Source Emplacement and Fault Zone Structure on Near-Source Wave Scattering

The comparison of our synthetic seismograms between shallow earthquakes and explosions using a velocity model with complex surface topography and heterogeneous shallow crustal structure with random perturbations showed that the effects of scattering on different types of waves could explain why in general P/S high frequency spectral ratio is a good tool for discriminating between earthquakes and explosions. Given the increased accumulated effects of scattering as a function of distance this discriminant could work better for longer distances. However there are cases where P/S ratio is not stable. One reason could be the anomalous wave propagation scattering caused by either strong near-source structural discontinuities such as basin edges with strong velocity contrast, fault zones with complex geometry, or near source topographical effects on waves generated from the source. Here we focus on basin edge effects and fault zone trapped waves effects on synthetic seismograms calculated at short and intermediate distances (30 -150 km).

7.1 Basin Edge Effects

Assessment of effects of near-source structure including micro-basins, surface topography, small-scale shallow heterogeneities, and source emplacement conditions on local and teleseismic waveforms.

In our investigation we used the 3D velocity model and receivers shown in Figure 10. We calculated two sets of synthetic seismograms (0.1-1.8 Hz) from an explosion source located near the basin edge, but outside the basin referred to as source RE and from another explosion source located near the basin edge inside the basin referred as source BE (Figure 15). Both sources have a depth of 400 m. The grid spacing in our finite difference calculations is 200 m. Figure 16 compares the corresponding vertical component of synthetic velocity band pass filtered at 0.1-1Hz and 1.0-1.8 Hz, frequency

12

bands, respectively. There are clear waveform differences between the two sources especially at high frequencies (1.0-1.8Hz). The most significant one is the difference in amplitudes of P waves and P coda waves. The explosion outside the basin produces much larger P waves that are rich in high frequencies. In contrast the amplitude of the P wave and P coda waves is relatively small for the basin explosion. This behavior could be explained by the trapping and diffraction of short period P waves in the basin edge. Meanwhile the structural complexity at the basin edge increases the energy of S coda waves mainly due to P to S waves conversions. Besides being attenuated in the basin sediments, the P wave do not develop much coda waves as some of their energy reflected at the free surface leaks back to the underlying bedrock and deeper crust and probably trapping and intrinsic attenuation. As a consequence the waveform from the basin explosion look very similar to these from an earthquake. Also the reduction of P/S ratio caused by basin edge effects makes it difficult to discrimination between the explosion and shallow earthquake. This is clearly seen in Figure 17 which compares smoothed envelopes of the vertical component of velocity at station S16 (rock site) and station S26 (basin site) calculated for an earthquake at a depth of 7 km, explosion located outside the basin, and explosion located within the basin. At high frequencies (1-1.8 Hz) there is a striking similarity between the earthquake and basin edge explosion in both rock site and basin site. Our simulation demonstrates that P/Rg ratio for explosion sources is sensitive to the source emplacement structural complexities. Our results suggest that P/S discriminants should be used with caution when the explosion source is located very near to a basin edge with strong velocity contrast, at least at frequencies less than 2 Hz.

7.2 Fault Zone Damage Effects

Fault zone effects on wave propagation have been observed and well recorded during large earthquakes. These observations reveal the complexity of the fault zone damage which could reach depths of 7-10 km. Depending on the structural complexities of the fault zone and age of the faults the obvious effects of wave trapping within the fault zone have been shown to be significant at high frequencies and near-fault distances. It is only recently that studies of fault zone effects have been extended to smaller events and at regional distances of interest for the nuclear explosion discrimination procedures. As we described in the previous section their observation shows that complex structure of tectonic regions not only affect the rupture dynamics it also affect the azimuthal distribution of radiated energy and rupture directivity. In addition, the effects are strong at high frequencies. The azimuthal dependency of this peculiar behavior need to be taken into account when broad band techniques are used to invert for focal mechanism and magnitude estimates of small events. Through 3D numerical simulations and using simple fault zone models we demonstrate the implication of fault zone damage on observed waveform scattering of P and S waves.

Figure 18 shows the locations of a vertical fault zone, earthquake epicenter and two circular arrays of stations used in the simulation of velocity seismograms. We used a grid spacing of 40m which ensured accurate modeling up to 7Hz. The fault zone is 700 m wide, and reaches a depth of 12 km. The softer material within the fault zone is represented by random perturbations of shear modulus up to 10% with a correlation length of 1 km. In order to investigate the effects of scattering due to the fault zone we

calculated velocity seismograms from a pure strike slip earthquake rupturing a 1kmx1km fault area. The rupture starts near the southern edge of the fault and propagates north. We considered three different fault locations similar to the ones observed during the Big Bear earthquake sequence. In the first scenario the fault is located in the middle of the fault zone. In the second scenario the fault zone is located outside the fault zone on the east side 200 m of the fault. The simulations for the third scenario were performed without the fault zone. The corresponding synthetic were used a reference in the analyses of the rupture scenarios with fault zone effects. The comparison of transverse and vertical components of simulated velocity seismograms (0.1-7Hz) are shown in Figure 19.

Two interesting wave propagation phenomena are observed when the fault ruptures within the fault zone: First, ringing of the S waves caused by waves trapped within the fault zone is visible only at receivers located in front of the north tip of the fault zone (receivers 5, 6, and 7). A less visible ringing is observed after the P wave. It is mainly caused by trapped P waves and P to S converted waves. Second, very pronounced surface waves with long coda propagate away from the fault tip. They dominate the coda waves behind the S wave train. A slight decrease in the duration of direct S wave pulse caused by the forward rupture directivity effect is seen at receiver 7.

These typical waveform characteristics are obviously not present when the fault zone is excluded, as demonstrated by the half space modeling results. When the earthquake ruptures adjacent to the fault zone the waveform complexities are still preserved. However the ringing phenomenon is weaker and the S coda waves at receivers on the opposite side of the fault zone are much smaller in amplitude. The most striking difference between the two scenarios is the duration of the direct S wave pulse. Our simulations suggests that when the earthquake is located within the fault zone the S wave pulse duration is much longer. Therefore S waves perturbed by the fault zone structure may not contain the correct information about the source rupture process. They tend to be contaminated by wave scattering which largely depends on the relative location of the fault with respect to the fault zone. Also our simulations suggest that the amplitude of coda waves from earthquakes near or in the fault zone depends on whether the fault zone reaches the free surface. Buried fault zones may not generate strong surface waves.

Our fault zone model is far for being realistic. Nevertheless it underlines the significant effect of the source region wave scattering in regions with fault damaged zones.

8. Rupture Directivity Effects in Media With Random Velocity Perturbation

Studies of local and regional waveforms from small earthquakes have demonstrated that rupture directivity has a significant effect on a broad frequency range. The forward rupture directivity affects the amplitude of seismic waves on a broad frequency range by increasing the amplitude of the ground motion in the direction perpendicular to the fault plane. In contrast at sites receiving the backward rupture directivity the ground motion

amplitude is greatly reduced but the duration of the signal is increased. There haven't been many studies of rupture directivity of small events especially at high frequencies. By using empirical Green's functions of small magnitude earthquakes, Tan *et al*., 2006 were able to derive the rupture process of earthquakes of the Big Bear sequence in the magnitude range m2.5. They found that the rupture directivity affects frequencies up to 7 Hz. These frequencies are within the range used in source discrimination studies.

In this study we investigate the effect of wave scattering on waveforms affected by rupture directivity during small earthquakes. We used two velocity models, one is an horizontally layered model (1D model) and the other one includes random perturbation of velocity in the upper 6 km of the horizontally layered model, and small shallow basins (3D model with scattering). The perturbations were designed to simulate wave scattering similar to the previous numerical experiments. We calculated synthetic waveforms from a double-couple point source with pure strike slip mechanism to maximize the directivity effect on the transverse component and an extended source containing 4 double-couple point sources with pure strike-slip mechanism, activated at equal time intervals to simulate unilateral rupture propagation. The sources are equally spaced by 400 m. The rise time is 0.15 sec, and rupture velocity is equal to 0.8times the local shear wave velocity. The maximum frequency in our synthetics is 6.5 Hz.

Figure 20a shows an overview of the top part of the model with locations of the source and stations. In this figure we also compare the fault-normal component of velocity seismograms for the extended source rupturing toward east and velocity seismograms for the reference double couple point source. The synthetic were calculated with the 1D model. Compared to the single point source model the extended source model generates synthetics with slightly reduced high frequency amplitudes, especially at receivers on the west of the source (rec: 6, 5, 4, 3, 2, an 1). This well-known phenomenon is caused by destructive wave interferences at high frequencies. At stations affected by the forward rupture directivity the pulses associated with the main phases become sharper enhancing the amplitude of high frequency phases.

Figure 20b shows the results of simulations for the 3D model with scattering. Scattering increases the time duration of the directivity pulse and reduces the high frequency energy of the signal at all stations. Although effective in reducing the high frequency energy at all receivers the wave scattering does not completely destroy the high frequency effects of rupture directivity. This is clearly shown in Figure 21 where we compare the amplitude Fourier spectra of the signal recorded at station 12 (forward rupture directivity) and station 4 (backward rupture directivity) for the 1D model and 3D-scattering model. In this figure we can clearly see that scattering reduces the amplitude of high frequency motion, but it does not modify the rupture directivity effects of rupture propagation which is expressed by the difference in waveform between motions at stations located in a direction toward the rupture propagation direction (station 12), and opposite to rupture propagation direction (station 4). This result demonstrates that in general rupture directivity effect expressed by the azimuthal changes of the S wave amplitude due to rupture propagation is not affected by wave scattering.

9. Seismic Source Discrimination

Empirical data from earthquakes and explosions have revealed that ground motions from explosions contain a considerable amount of S wave energy, and that the ratio of P/S spectra could be used as a stable discriminant (e.g., Walter *et al.*, 2007). Theoretically, we expect S-waves from explosions to be weak at all frequencies since they can only come from pS waves, assuming the usual simple 1D modeling. Since the surface generally has low velocities, this conversion of wave-types is small, therefore a flat free-surface has a small contribution to S wave energy. It is important to know how some explosions generate shear wave energy. Some explosions are best modeled with CLVD's (e.g., Patton 2007), suggesting that S wave energy is generated at the source. Near-in data suggests such contributions as well, Saikia, 2006. Kennedy (1982) discusses the difference between two Rainier Mesa Tunnel events in terms of block motion. We intend to address these issues by modeling NTS events with known source region surface complexities.

Recent investigation of factors that affect the spectral content of S waves during explosions based on analyses of recorded data and two-dimensional numerical modeling suggest that a large portion of S waves is created as a result of P to S wave conversion at the free surface as well as wave scattering in the source region (e.g., Mc Laughlin *et al.,* 1986). Due to complexities in the surface structure, including topography and micro-basins, the free-surface reflection coefficients for different waves become complex. Because of wave interference the frequency content of the primary waves is altered, thus leading to modifications in the spectrum of the source-originated P and S waves. This means that the observed P/S spectral ratio depends not only on the source type but also on surface and underground complexities of the medium surrounding the source. Neglecting the effect of these complexities may cause inaccurate yield estimates, and makes the P/S spectral ratio discriminant ambiguous at certain frequencies. It is therefore very important to understand and quantify the effects of interaction between primary waves with the source-emplacement structural complexities during explosions.

In an effort to study waveform differences between earthquakes and explosions we extend the frequency range of our 3D modeling to higher frequencies by performing numerical simulations of wave scattering using a regional 3D velocity model of the crust with flat topography. The exclusion of the topography allows the calculation of full waveforms at regional distances up to 350 km and frequencies up to 3.5 Hz. All simulations were performed on the computer cluster at Caltech using 300 – 400 nodes. We calculated full seismograms using a double couple point source at 2 km depth with an arbitrary focal mechanism, and an isotropic explosion point source at 500m depth. Figure 22 shows a map view of the crustal velocity model used in our simulations. The crustal 3D velocity model includes flat layers and large scale and small-scale structural heterogeneities.

The comparison between the earthquake source and explosion is shown in Figure 23. In this figure we compared vertical component seismograms calculated at a linear array of stations showed in Figure 22, band –pass filtered at 0.1-3.5Hz and 2.0-3.6 Hz. All

synthetics are scaled to unit maximum amplitude in order to facilitate the comparison between P, S and Lg coda waves in each seismogram. As in previous models with surface topography, the generation of secondary S waves and S and Lg coda waves for the isotropic explosion source is impressive. The wave propagation scattering can produce Lg, P and S coda waves with significant energy even for isotropic explosion sources. Other simulations performed with the same scattering model confirm that the energy of Lg coda waves increases when the source depth decreases. An even more drastic effect was seen for the P coda waves. The explosion waveforms are dominated by high frequency P coda waves and low frequency Lg coda waves (Figure 23a). At high frequencies the relative energy of P and Lg waves starts to show significant differences between the explosion and earthquake (Figure 23b). The P/L ratio is much larger for the explosion. The difference of P/Lg ratio between the explosion and earthquake at high frequency is controlled more by P rather than Lg waves. As demonstrated by our simulation the energy of Lg coda waves for both explosion and deep earthquake sources are very similar. At longer distances P waves generated by the explosion become richer in high frequency energy compared with the P waves coming from the earthquake source (see Figure 23a). This is probably due to the fact that for shallow sources P and converted P to S waves remain trapped within the scattering structure of the shallow crust. In contrast P waves coming from a deeper source, besides being attenuated, do not develop much coda waves as some of their energy reflected at the free surface leaks back to the deeper crust.

Another interesting characteristic of P waves is the P(high.freq.)/P(low.freq.) ratio. Our simulations suggests that P(high.freq.)/P(low.freq.) for the explosion is different from that of the earthquake. Using the simulated waveforms we estimated the P(2-3.5Hz)/P(0.1-1.0Hz) and P(2-3.5Hz)/Lg(2-3.5Hz) ratios at 95 sites. The time window used for the P wave includes the direct P and P coda waves. The comparison of these ratios between the explosion and earthquake is shown in Figure 24. Our result shows that for structures with shallow wave-path scattering P(high.freq.)/P(low.freq.) ratio can be used as a discriminant between earthquakes and explosions at short distances. At long distances its performance is poor. In contrast P/Lg ratio at high frequencies could be a good discriminant at longer distances. At low frequencies and short distances P/Lg ratios are very similar for shallow explosions and earthquakes. As shown in Figure 24 a good discriminant that works for all distances could be the combination of P(2-3.5Hz)/P(0.1-1.0Hz) and P(2-3.5Hz)/Lg(2-3.5Hz) ratios. This combination works well in particular for the vertical component which is more affected by the 3D wave propagation scattering and free surface topography.

Our numerical experiments with 3D velocity models that include random velocity perturbations and microbasins, representing wave scattering in the upper 5km of the crust, clearly show that wave-path scattering is a major contributor to S and Lg coda waves from explosions. The energy of Lg coda waves depends on the source depth. P/Lg ratios estimated at different frequencies indicate that this ratio could be a good discriminant between explosions and earthquakes when calculated at high frequencies. P/Lg ratios below 1Hz are very similar for shallow explosions and deeper earthquakes

10. DISCUSSION AND CONCLUSIONS

-Source Radiation pattern of P waves can be observed at frequencies as high as 8Hz.

-P-S conversions contribute to significant increase in amplitude of P coda waves in the tangential component at high frequencies.

-S waves are more susceptible to wave propagation scattering. The radiation pattern effect of S waves is largely distorted at frequencies above 2 Hz. At these frequencies the amplitude of all three components becomes the same. This suggests that at high frequencies the amplitude of S wave coda does not follow the source radiation pattern. This example shows that at high frequencies the S wave radiation pattern is mainly controlled by wave scattering in the crust. This very robust feature of S coda waves could be used to derive stable estimates of source parameters.

-The comparison of waveform envelopes between an earthquake and North Korean show that along long wave path and due to wave scattering the P/S ratios between the earthquake and explosion are very different. P/S ratio for the explosion at MDJ is much larger. These observations suggest that at large epicentral distances the cumulative effect of wave scattering on P/S coda wave ratio is enhanced. Therefore at large distances the P/S coda wave ratio could be a good discriminant between earthquakes and explosions. This observation is very well reproduced by our subsequent simulations of 3D wave scattering.

- Near-source wave scattering has a great implication in shaping the source energy radiation at local and teleseismic distances. It also affects the amplitude of depth phases. The analyses of the Big Bear earthquake sequence by Tan *et al*., 2006 and results of our simulations of fault zone trapped waves demonstrate that wave propagation scattering in the fault damage zone causes very complex waveforms. The small-scale heterogeneities affect the S waves more than the P waves which have longer wavelengths. Here we argue that this feature is caused by fault-zone damage where energy is locally trapped in the slow leaky waveguide and then re-radiated from the lateral edges of the fault zone. Our 3D numerical simulation demonstrates the implication of fault zone damage on observed waveform scattering of P and S waves.

- A significant improvement in the 3D finite-difference technique was made by the application of the finite-difference operators on 3D grids with variable spacing (Pitarka 1999). This, combined with parallel processing, enables the modeling of wave propagation at high frequencies using realistic crustal velocity models. Our 3D-FDM computer code solves the stress-velocity equations in a heterogeneous medium using staggered grids based on such technique. The code can also treat heterogeneous structure with surface topography and rupture dynamics as well (Pitarka and Irikura, 1996, and Pitarka and Dalguer, 2003). The technique is an excellent approach to modeling complex wave propagation in regional settings.

- Our numerical technique for simulating 3D wave propagation scattering through random velocity perturbations and surface topography constraint by observed P and S coda waves amplitude, and coda wave decay, produces realistic waveforms.

- We have examined combined effects of wave propagation scattering due to complexities in the shallow crust and surface topography in relation with the source depth. Our simulation result suggests that in relation with the source depth high frequency scattering is more stable than the low frequency scattering. The slope of high frequencies envelope does not depend on the source depth. In contrast the slope of the low frequency envelope depends on the source depth. Therefore the slope of the smoothed envelope of the low frequency part of the signal could be used to discriminate between shallow and deep events.

- Our simulation of shallow earthquakes and explosions suggests that the amplitude ratio between P and Rg coda waves is still higher for the explosion source at high frequencies. This important characteristic is used in developing a stable discrimination technique. Our simulations clearly show that because S coda waves have shorter wavelength their amplitude diminishes faster than that of P coda waves at long distances. This means that in general P/S type discriminants may work better for longer distances. This result is in agreement with similar observations made when we compared the North Korean explosion and a nearby earthquake at short and regional distances. P coda waves from the explosion have relatively large amplitudes compared to P coda waves from the earthquake. The cumulative effect of scattering caused by the surface topography and spatial structural heterogeneities contribute to generation of P coda waves through P/S and S/P conversions. Contrary to low frequencies, at high frequencies the difference of P/Rg ratio between the explosion and the earthquake source is significant. Our simulations demonstrate that the P/Rg wave ratio could be a good discriminant between the earthquake and explosion sources.

- Assessment of effects of near-source structure including micro-basins, surface topography, small-scale shallow heterogeneities, and source emplacement conditions on local and teleseismic waveforms. Our simulation demonstrates that P/Rg ratio for explosion sources is sensitive to the source emplacement structural complexities. Our results suggest that P/S discriminants should be used with caution when the explosion source is located very near to a basin edge with strong velocity contrast.

- Our simulations of fault zone damage effects suggest that when the earthquake is located within the fault zone the S wave pulse duration increases. Therefore S waves perturbed by the fault zone structure may not contain the correct information about the source rupture process. They tend to be contaminated by wave scattering which largely depends on the relative location of the earthquake with respect to the fault zone. Also our simulations suggest that the amplitude of coda waves from earthquakes located near or in the fault zone depends on the fault zone orientation and whether the fault zone reaches the free surface. Buried fault zones may not generate strong surface waves.

- Scattering reduces the amplitude of high frequency motion, but it does not modify the rupture directivity effects of rupture propagation which is expressed as difference in waveform between motions at stations located in a direction toward the rupture propagation direction, and opposite to rupture propagation direction. This result demonstrates that in general rupture directivity effect expressed by the azimuthal changes of the S wave amplitude due to rupture propagation is not affected by wave scattering.

19

Instead it remains visible in a broad frequency range as shown by Helmberger *et al*., 2008.

- Our numerical experiments with 3D velocity models that include random velocity perturbations and microbasins, representing wave scattering in the upper 5km of the crust, clearly show that wave-path scattering is a major contributor to S and Lg coda waves from explosions. The energy of Lg coda waves depends on the source depth. P/Lg ratios estimated at different frequencies indicate that this ratio could be a good discriminant between explosions and earthquakes when calculated at high frequencies. P/Lg ratios below 1Hz and short distances are very similar for shallow explosions and deeper earthquakes. At short distances and structures with shallow wave-path scattering our simulations suggest that P(high.freq.)/P(low.freq.) ratio can be a good discriminant.
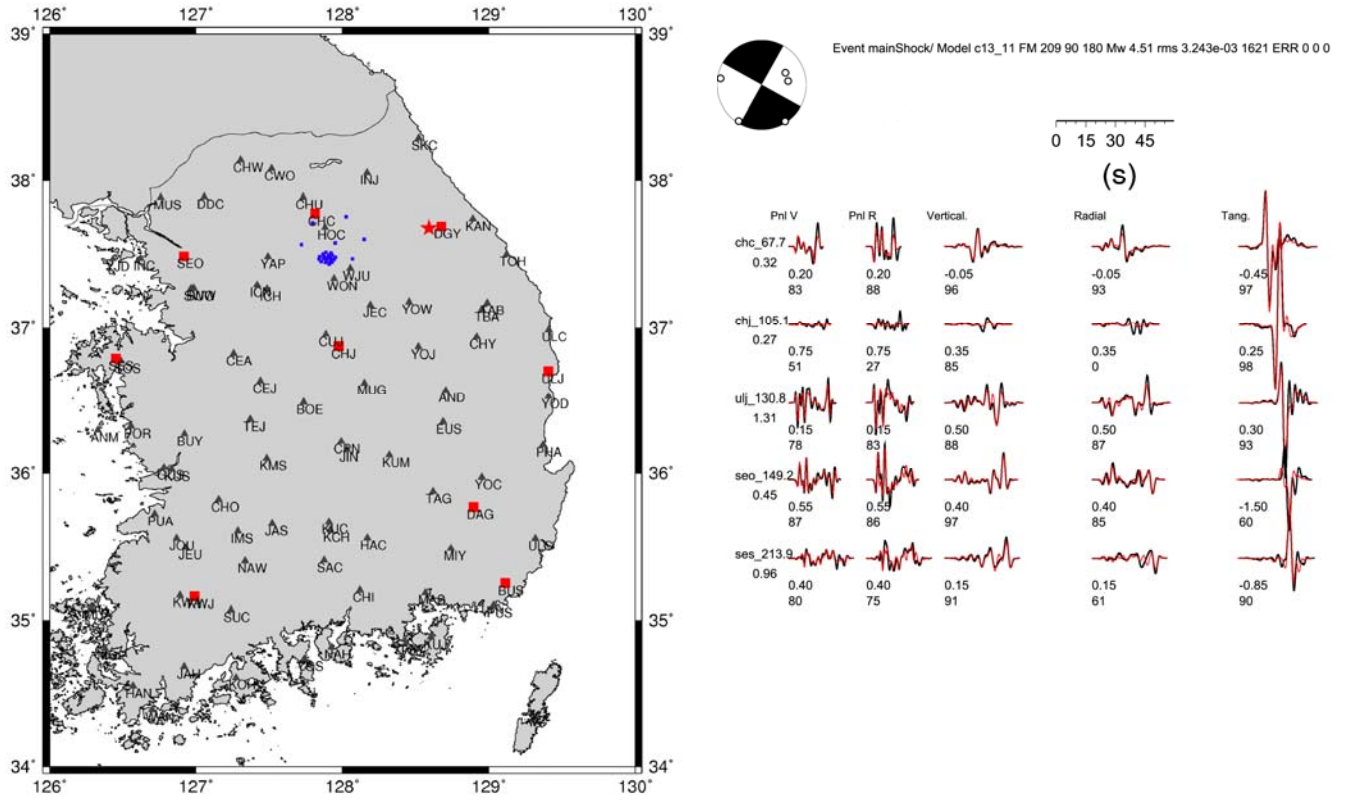
Figure 1. (Left panel) Map showing broad-band (red square) and short-period strong motion (black triangle) stations in South Korea. Blue squares show IMS (KSRS) stations, and the red star indicates the epicenter of the Mw4.5 070120 earthquake analyzed in this study. (Right panel) Focal mechanism of the earthquake and waveform fit obtained with a cut and paste (CAP) inversion technique.
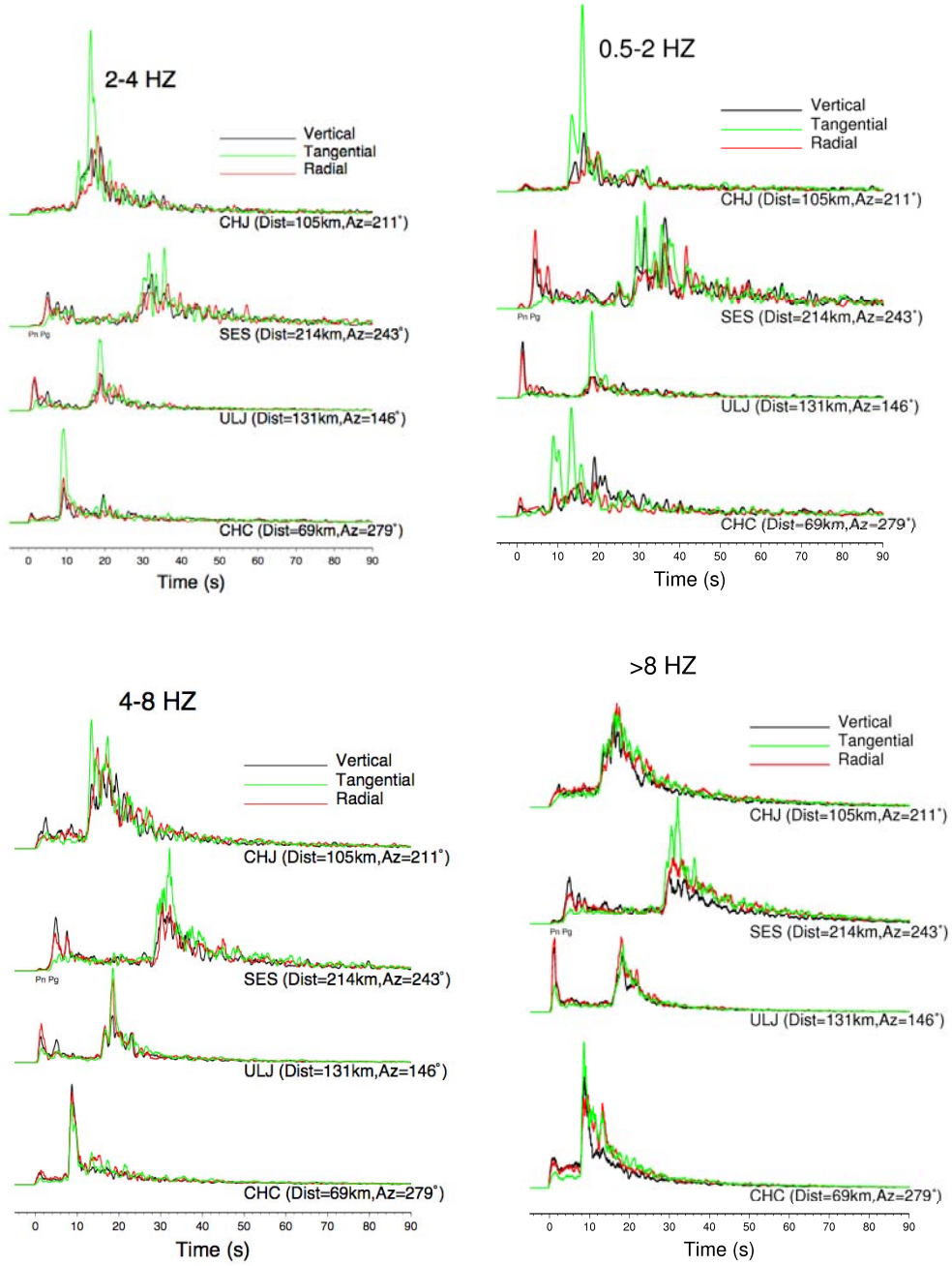
Figure 2. Smoothed envelopes of broad-band velocity seismograms recorded at station CHJ, SES, ULJ, and CHC from the Mw 4.5 070120 earthquake in South Korea. The envelopes are calculated at four frequency bands indicated on top of each panel.
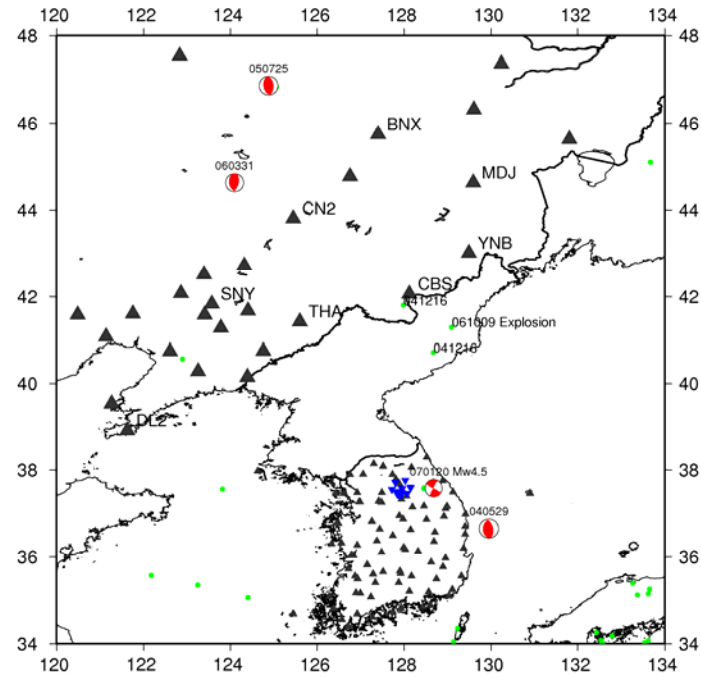
Figure 3. Map of southeastern China and Korea Peninsula. Triangles indicate broadband and short period stations of the China Seismic Network and Korean Seismic Network. The 061009 explosion and 020416 earthquake located in the Korean peninsula, and analyzed in this study are shown by green dots.
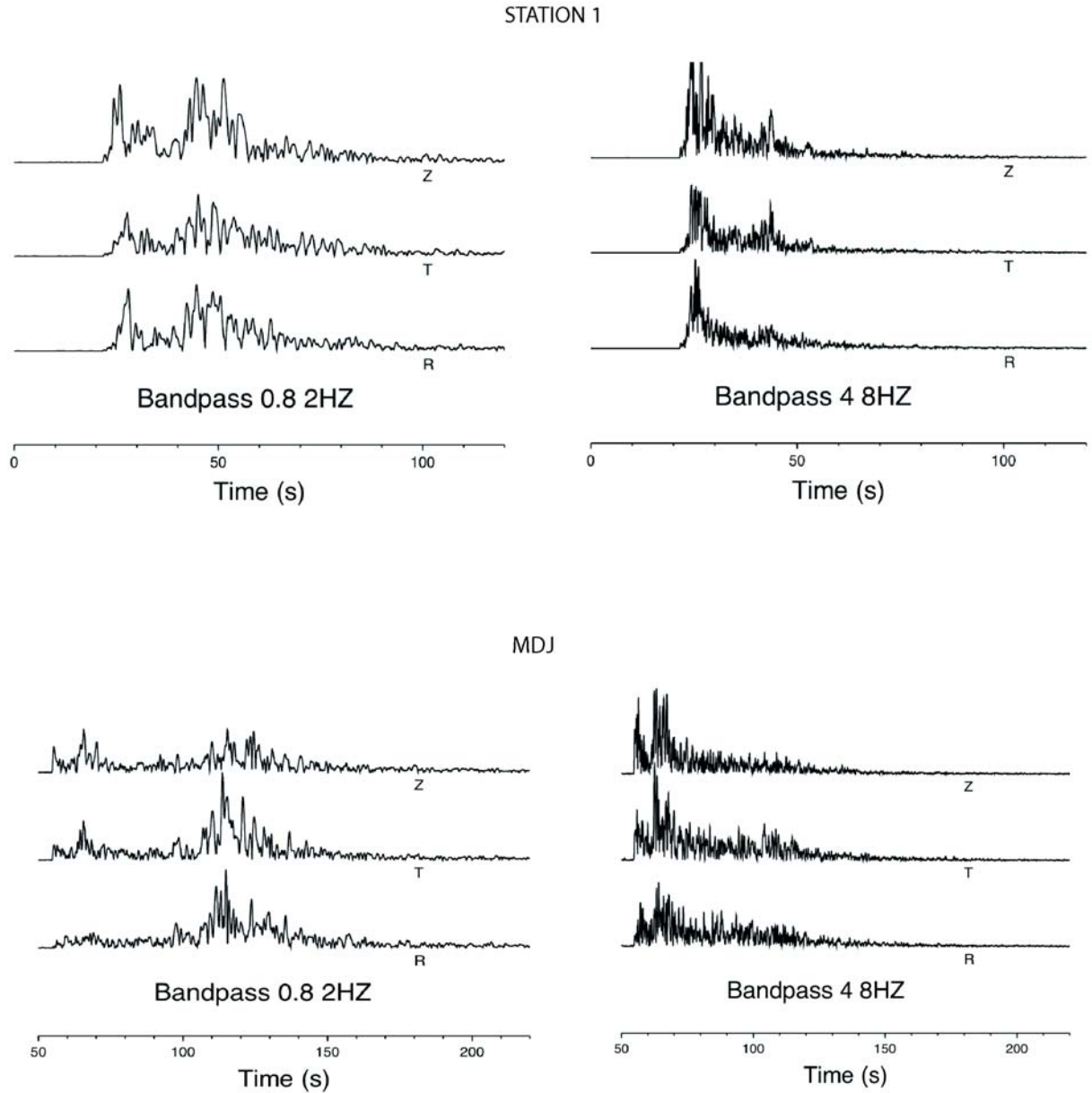
STATION 1

MDJ
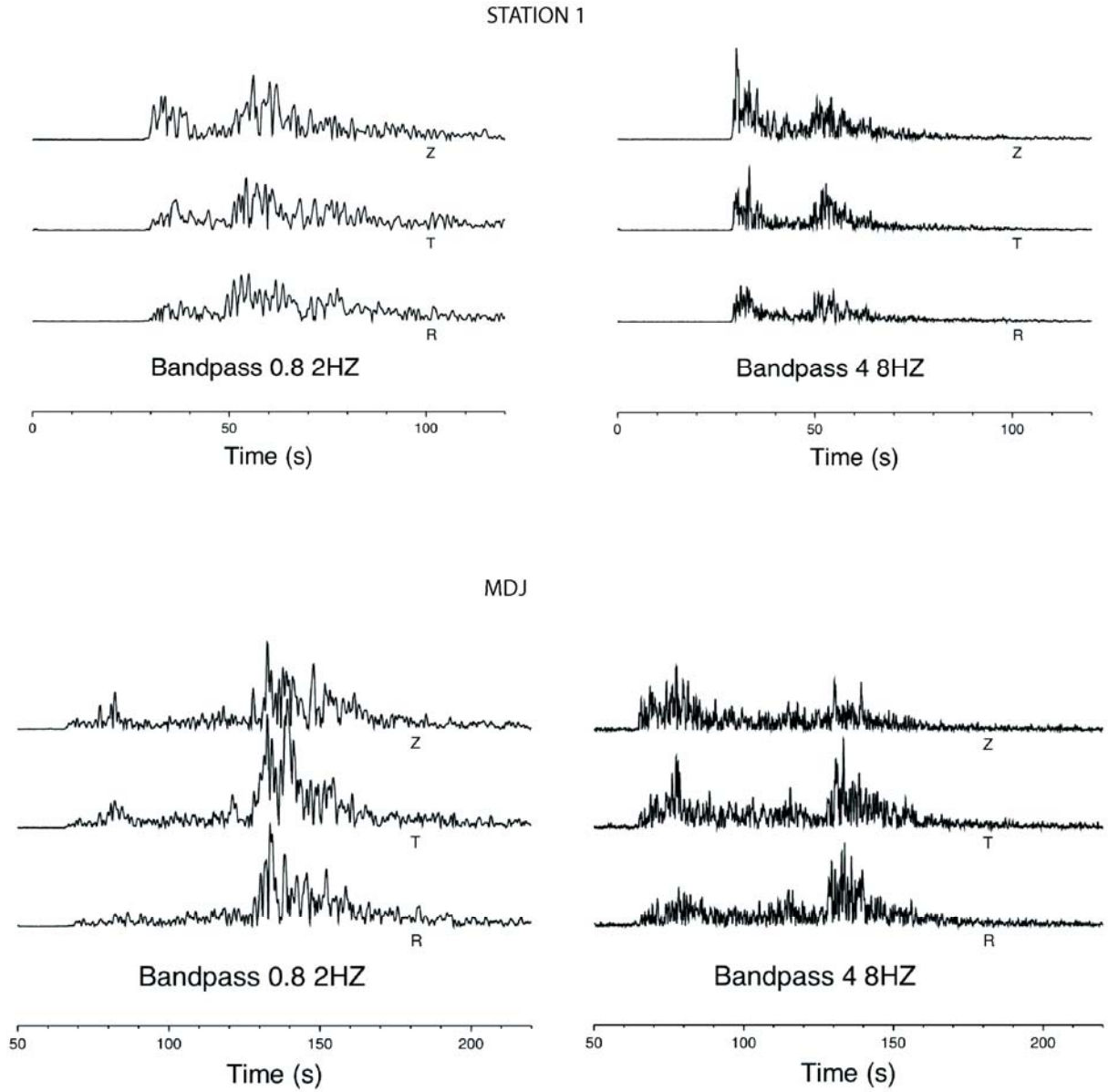
Figure 4a. Smoothed envelopes of velocity seismograms from the 020416 earthquake in North Korea recorded at STATION 1 (top panels) and MDJ (bottom panels) in the frequency ranges 0.8-2Hz and 4-8Hz.

Figure 4b. Smoothed envelopes of velocity seismograms from the 061009 North Korean explosion recorded at STATION 1 (top panels) and MDJ (bottom panels) in the frequency ranges 0.8-2Hz and 4-8Hz.
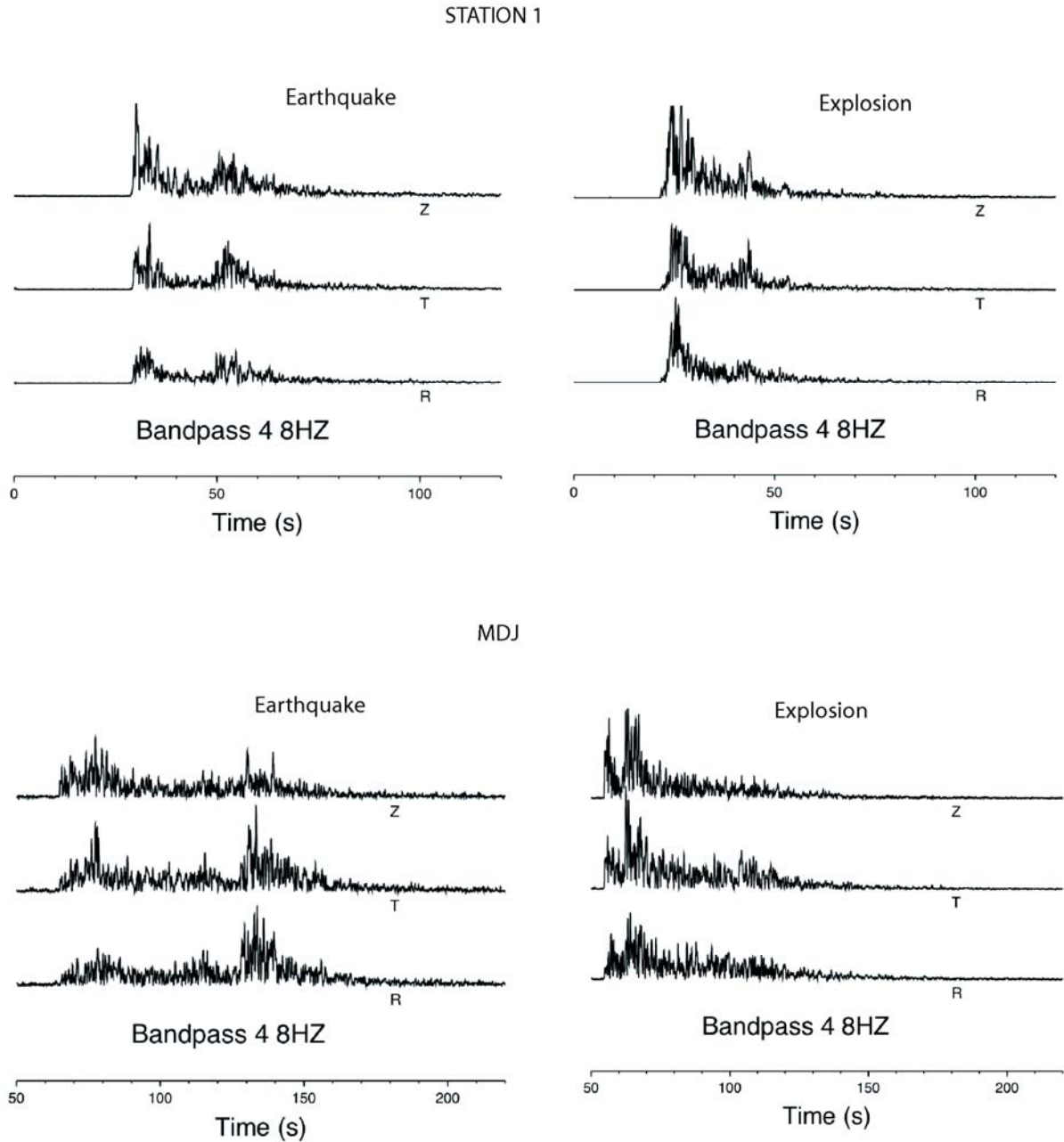
STATION 1

Earthquake

Z

T

R

Bandpass 4 8HZ

0   50   100

Time (s)

Explosion

Z

T

R

Bandpass 4 8HZ

0   50   100

Time (s)

MDJ

Earthquake

Z

T

R

Bandpass 4 8HZ

50   100   150   200

Time (s)

Explosion

Z

T

R

Bandpass 4 8HZ

50   100   150   200

Time (s)

Figure 4c. Comparison of smoothed envelopes of velocity seismograms at STATION1
and MDJ from the 020416 earthquake (left panels) and 061009 explosion (right panels)
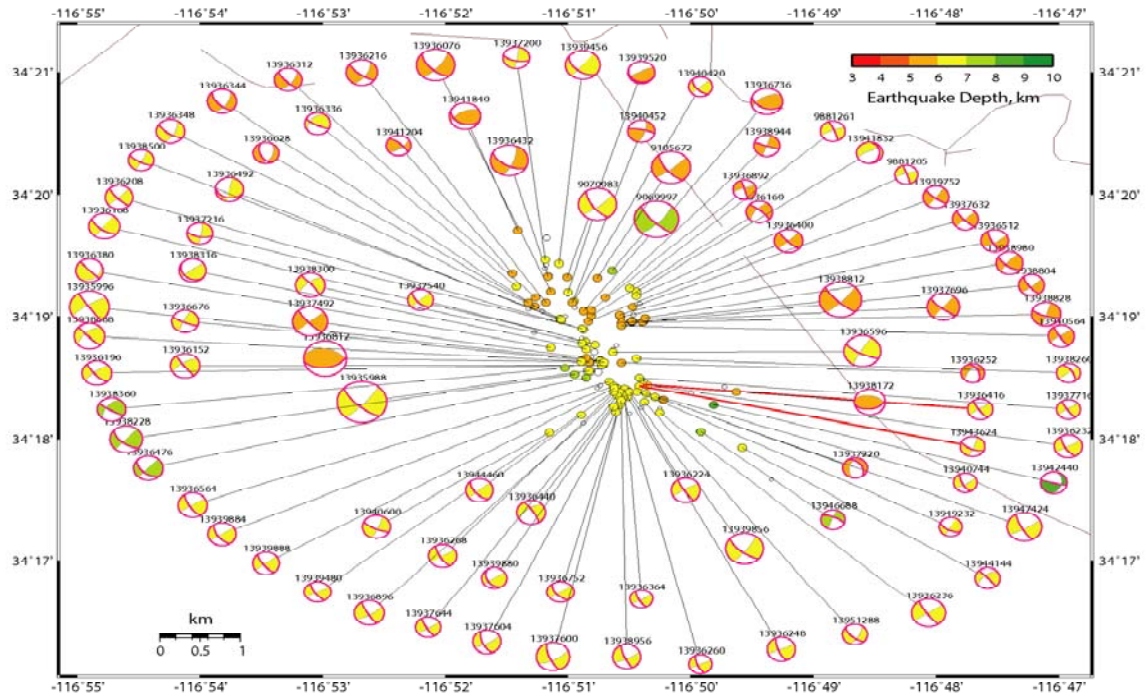in North Korea band-pass filtered at 4-8 Hz.

26

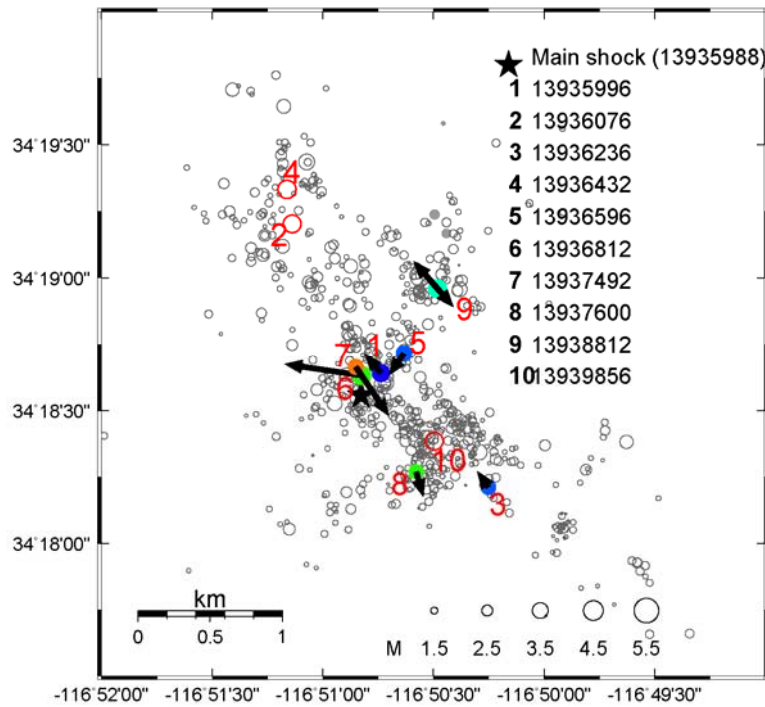Figure 5. Focal mechanisms of the Big Bear earthquake sequence

Figure 6. Inferred rupture directivity (arrows) for selected events and relocated seismicity. The event with reliable rupture parameters are color coded depending on the estimated stress drop. The arrow points to the rupture direction while their length is proportional to the estimated fault length.
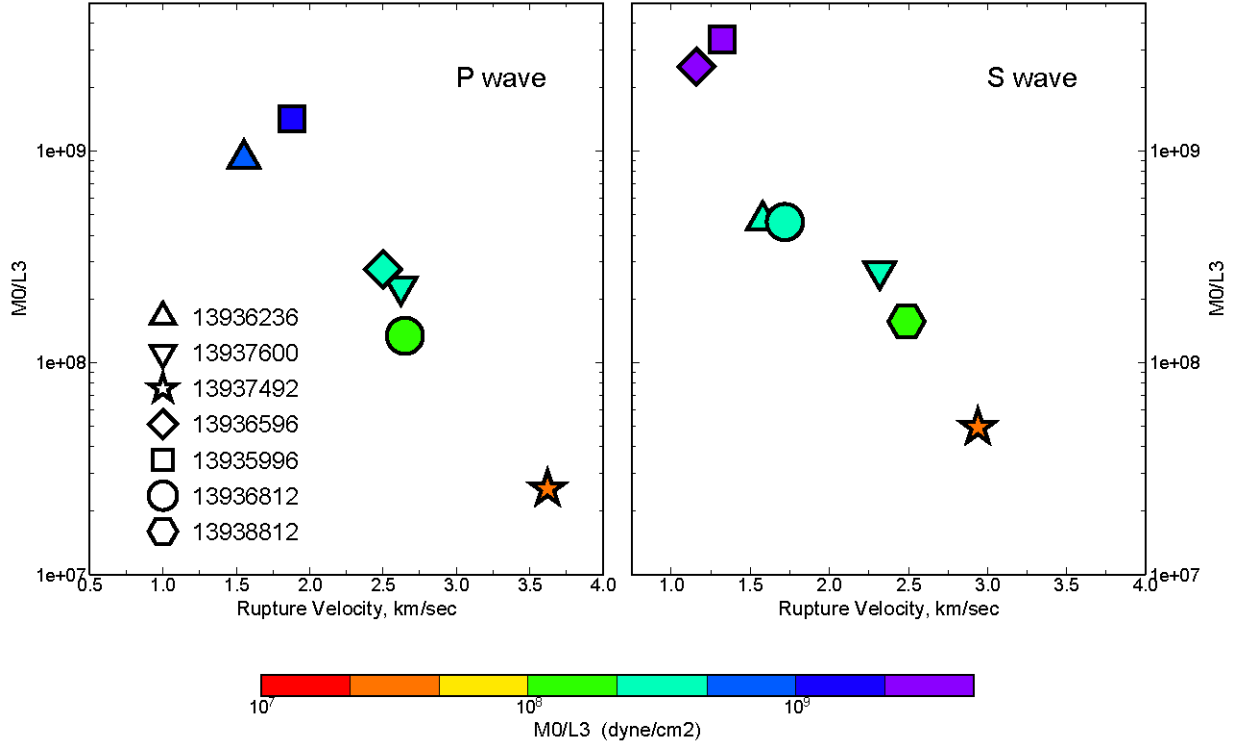
Figure 7. M_0/L^3 *vs.* V_r from the studied events. The results from *P* wave are displayed in the left whereas the *S* wave results in the right. Note the apparent anti-correlation between our estimated M_0/L^3 and V_r as displayed. Such inverse proportionality of $\Delta\sigma$ to Vr is consistent with the scale dependent $\Delta\sigma V_r^3$ predicted by Kanamori and Rivera (2004), although with the limited data points, we are not able to examine the moment dependence of $\Delta\sigma V_r^3$. It appears that events with low $\Delta\sigma$, likely on weak faults, tend to propagate at high V_r; whereas events with high $\Delta\sigma$, likely on strong faults, propagate at low V_r.

After Inter Correlation

Before Inter Correlation
S wave

40　　　　　　　　　　　　45

Station DPP (AZ=184) Events: 13936326 (red) 13937600 (green)

After Inter Correlation

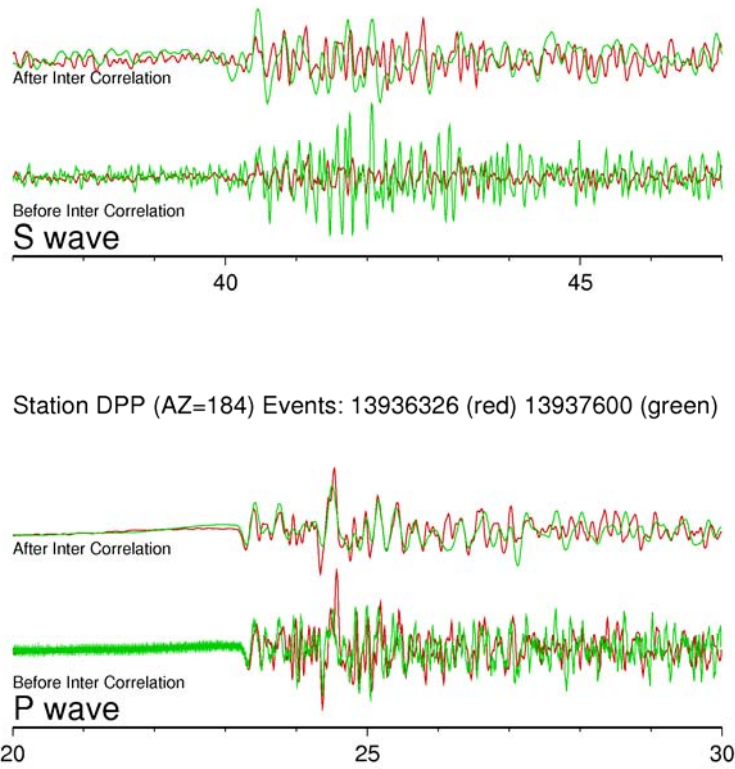Before Inter Correlation
P wave

20　　　　　　　　25　　　　　　　　30

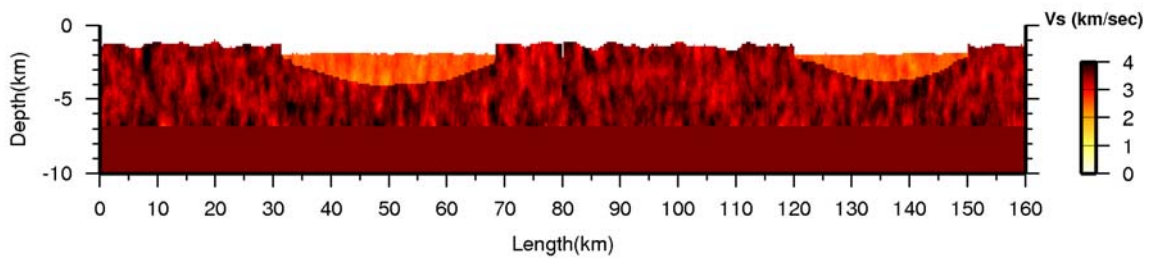Figure 8. Intercorrelations between recordings of two small events at DPP using S waves (top panel) and P wave (bottom panel).

Figure 9. Velocity model with smooth topography used in simulations of wave propagation scattering. Cross-section of the top 7 km of velocity model along the source-station linear array. The velocity is randomly perturbation in the upper 5 km of the crust. The maximum elevation is 1400m with a correlation of 3 km. The maximum velocity perturbation is 10% and the correlation length of perturbations is 1.5 km. Note that there is a factor of 3 vertical exaggeration.
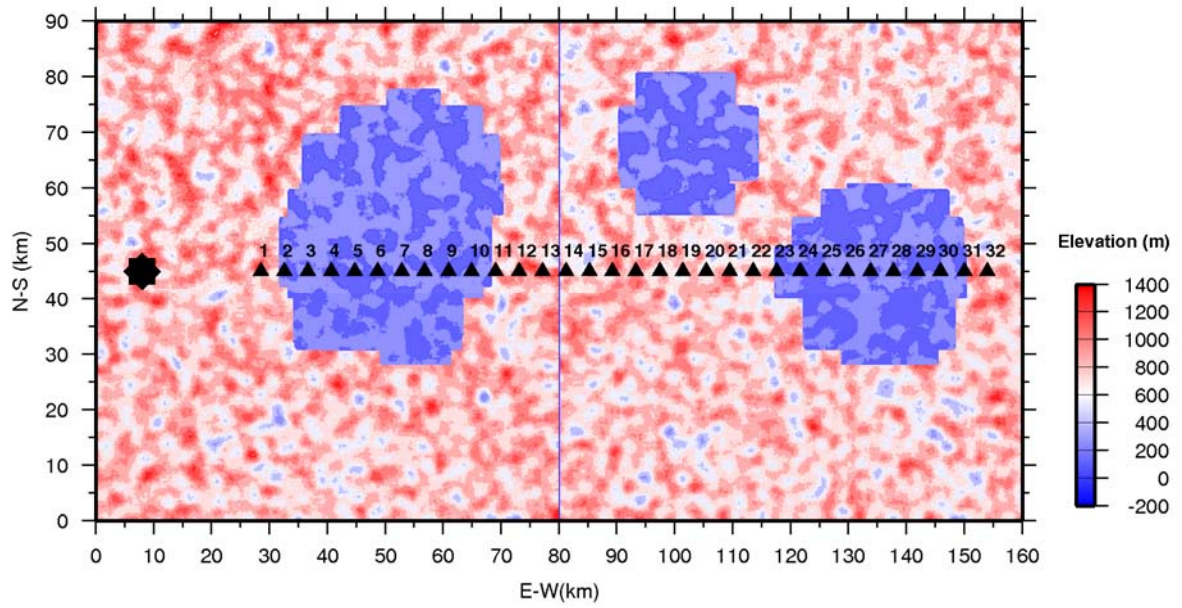
Figure 10. Display of topographic elevation. Triangles indicate stations, and star indicates the epicenter location.
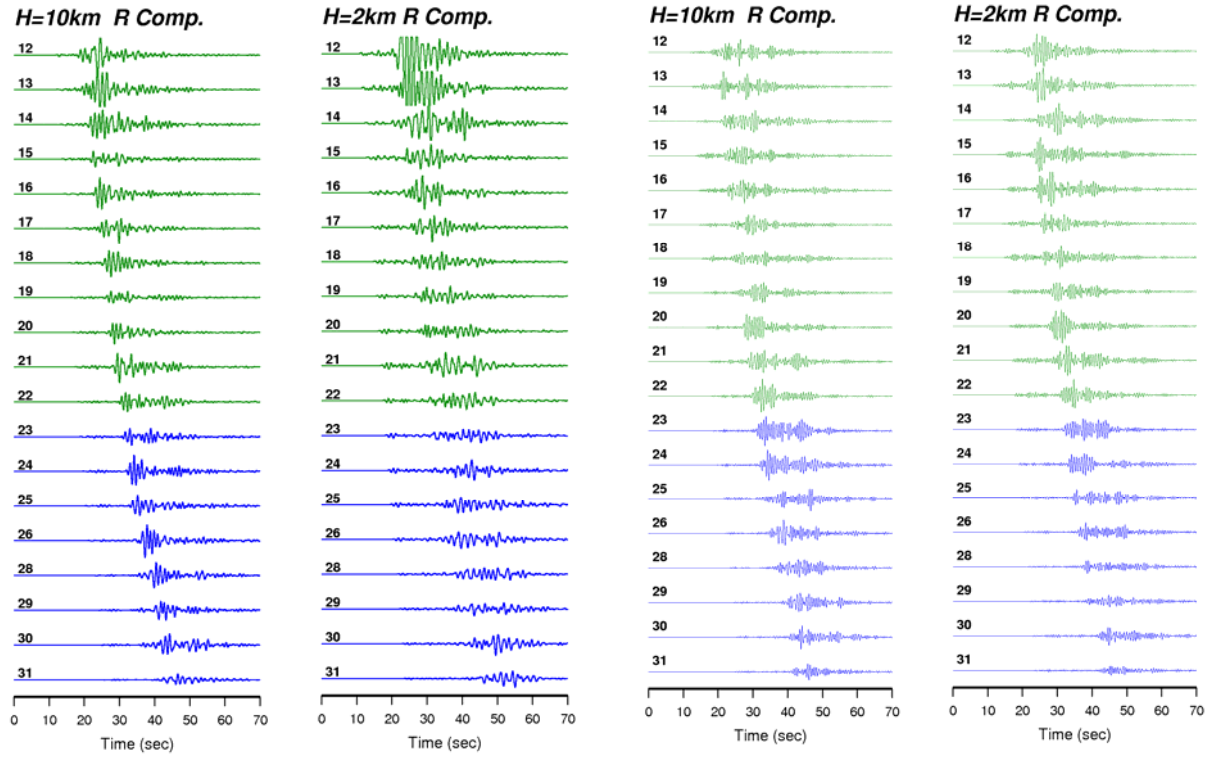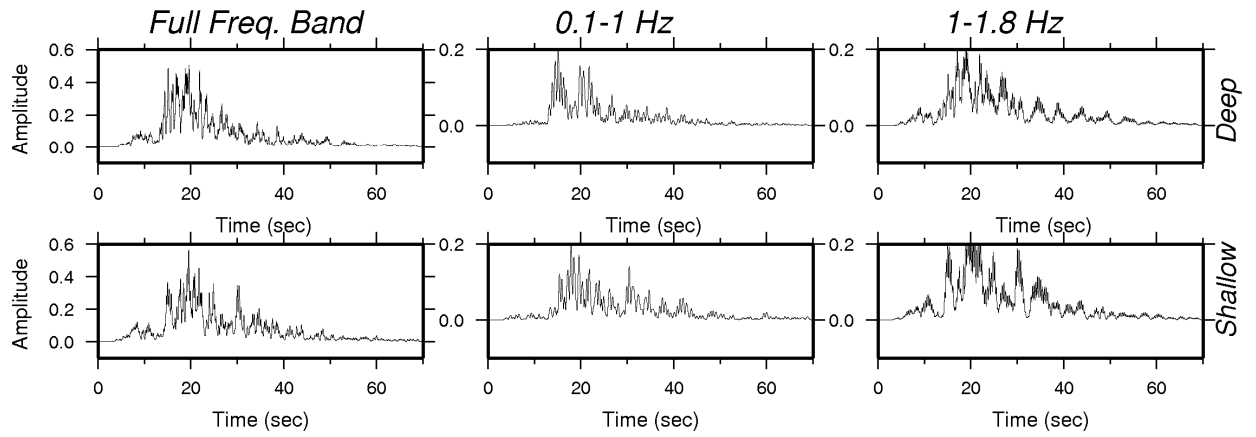
Figure 11. Vertical component of synthetic velocity for a strike-slip double-couple point source located at depths of 10 km (left panel) and 2 km (right panel). The synthetic seismograms are calculated with a 3D model that includes shallow crustal scattering effects (shown in Figure 10). The synthetics are band-pass filtered at 0.1-1.0 Hz. (two left panels), and at 1.0-1.8 Hz. (two right panels). Green traces correspond to rock sites, and blue traces correspond to basin sites.

S#16 Rock Site

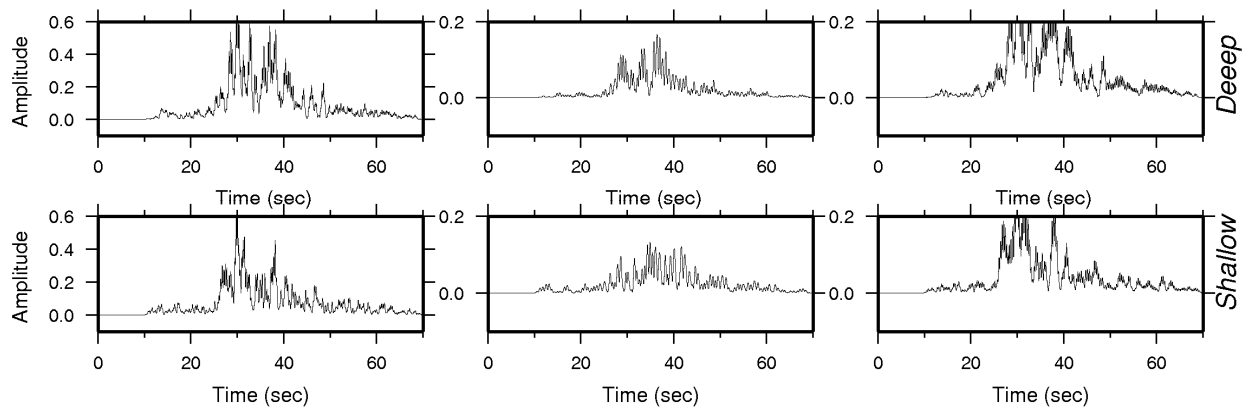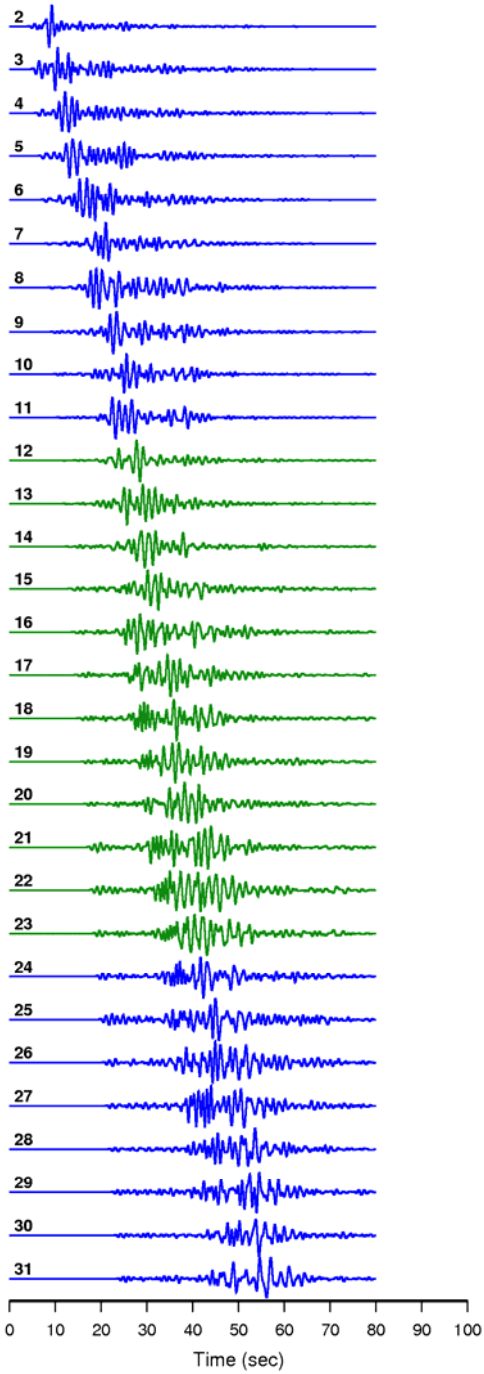| *Full Freq. Band* | *0.1-1 Hz* | *1-1.8 Hz* |

S#26 Basin Site

Figure 12. Smoothed envelopes of synthetic seismograms at sites S16 and S26. The envelopes are calculated using the vertical component of synthetic velocity seismograms band-pass filtered at 0.1-1.8 Hz (left panels), 0.1-1 Hz (middle panels), and 1-1.8 Hz (right panels).
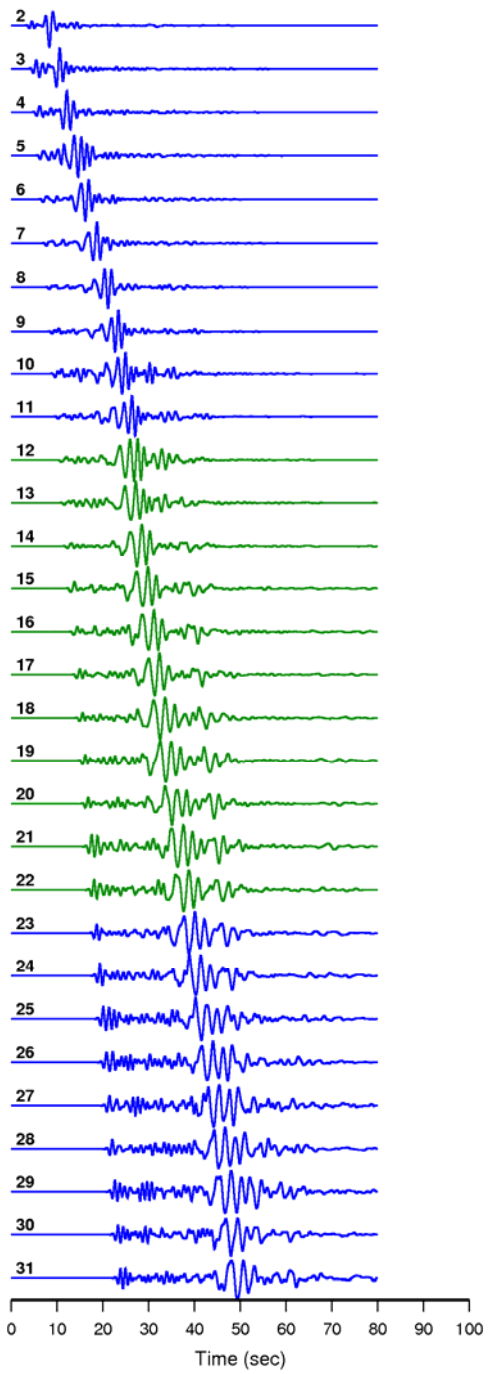
Figure 13a. Vertical component of synthetic velocity for a strike-slip earthquake with the source depth of 2 km (left panel), and isotropic explosion source at a depth of 0.4 km (right panel) band-pass filtered at 0.1-1.0 Hz. The synthetics are scaled to their individual maximum amplitude in order to facilitate the amplitude comparison between P and S waves at each station. Blue traces correspond to basin sites and green traces correspond to rock sites.
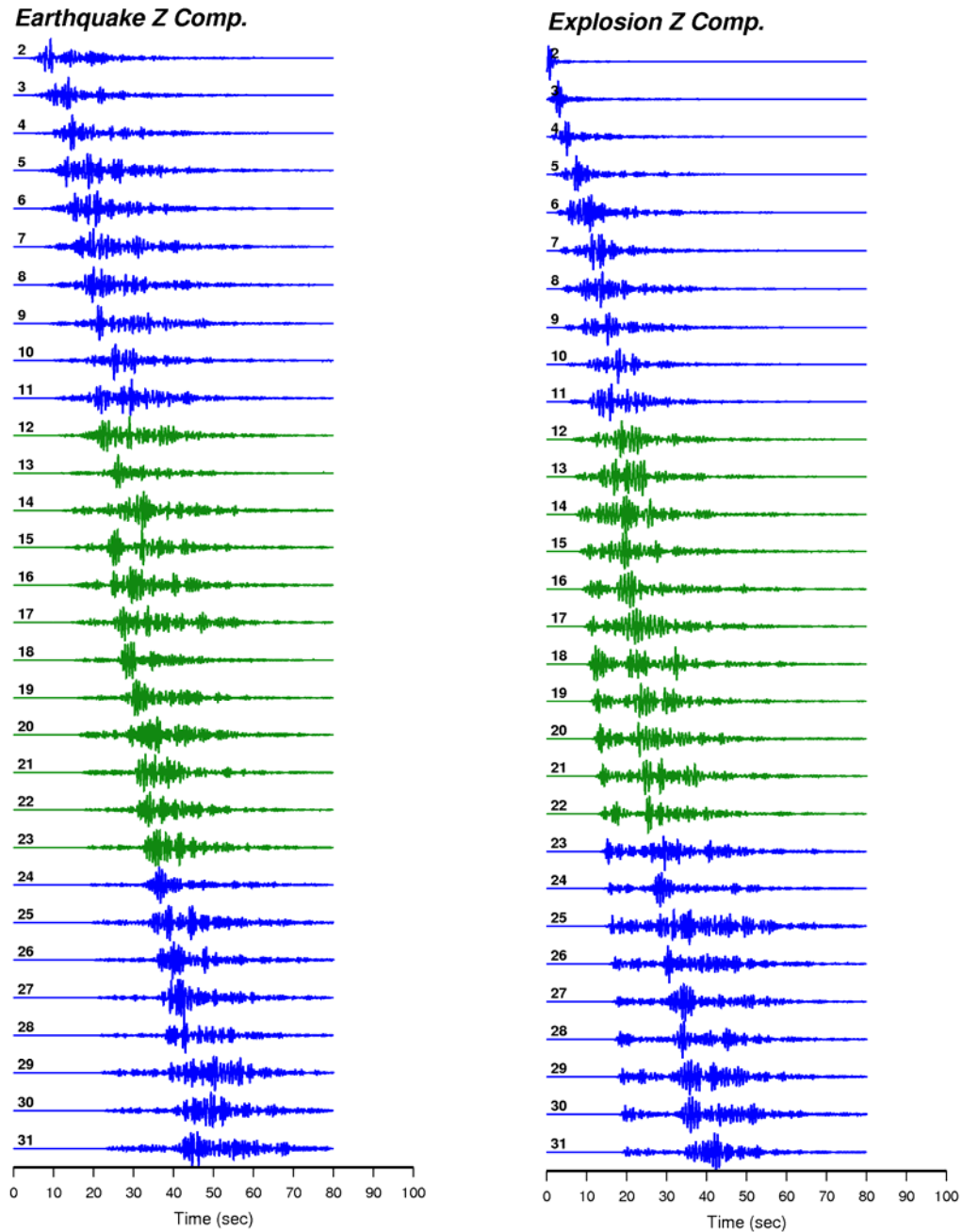
33

Figure 13b. Same as Figure13a but band-pass filtered at 1.0-1.8 Hz. The synthetics are scaled to their individual maximum amplitude in order to facilitate the amplitude comparison between P and S waves at each station.
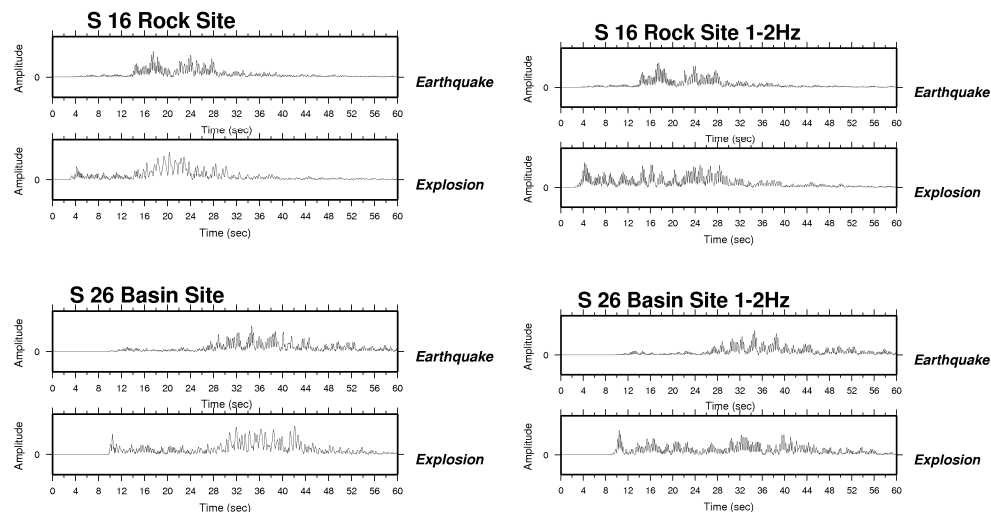
Figure 14. Comparison of smoothed envelopes for the vertical component of synthetic velocity seismograms at a rock site (station 16) and basin site (station 26) for the earthquake and explosion sources, band-pass filtered at 0.1-1 Hz (left panels), and 1-1.8 Hz (right panels). Note the relatively large P/S ratio of coda waves for the explosion in the frequency band 1-1.8 Hz. The simulated P/S ratio increases with the frequency. This is in good agreement with observation.
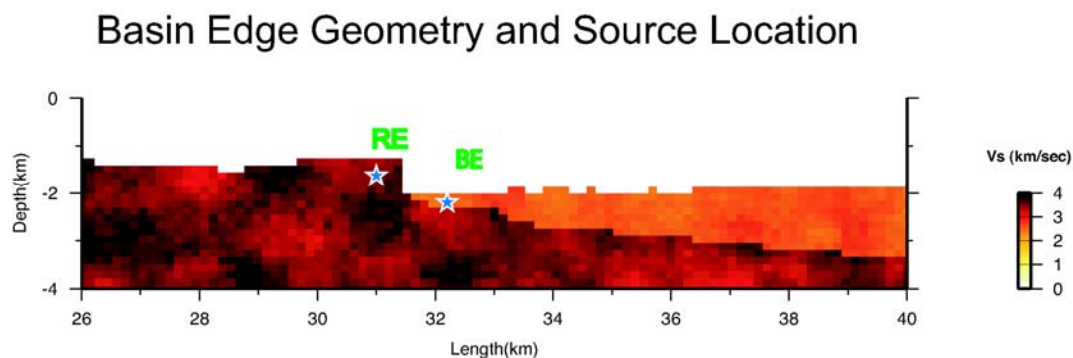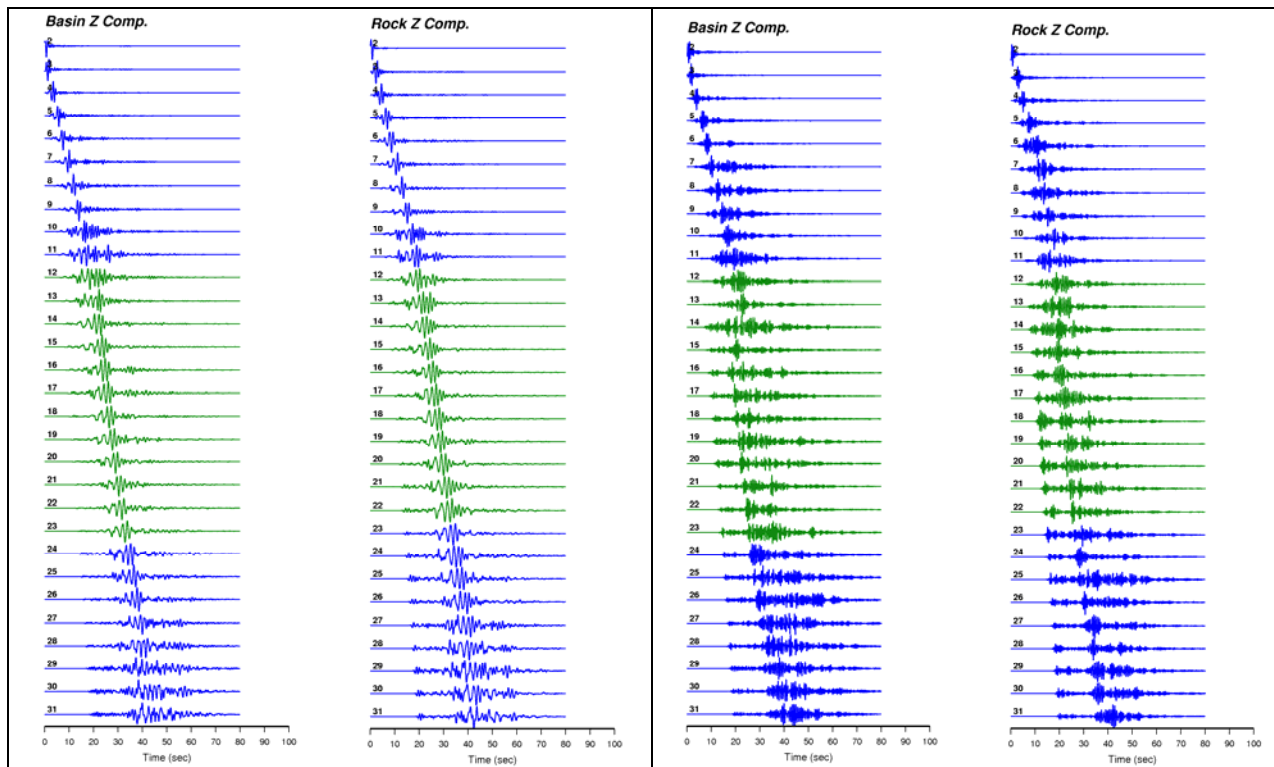

Figure 15. Close up of the velocity model in the region near the basin edge. Blue stars indicate the location of the explosion sources in rock near (RE) and in the basin sediments (BE) used in the simulations.

Basin Edge　　　　**Rock**　　　　**Basin Edge**　　　　**Rock**

(0.1-1.0 Hz)　　　　　　　　　　**(1.0-1.8)Hz**

Figure 16. Vertical component of synthetic seismograms calculated at the linear array shown in Figure 10. for an explosion source embedded in rock adjacent to the basin (Rock), and an explosion source embedded in basin sediments next to the basin edge (Basin Edge). Left panels show synthetic seismograms band-pass filtered at 0.1-1.0 Hz, and right panels show synthetic seismograms band-pass filter at 1.0 -1.8 Hz.
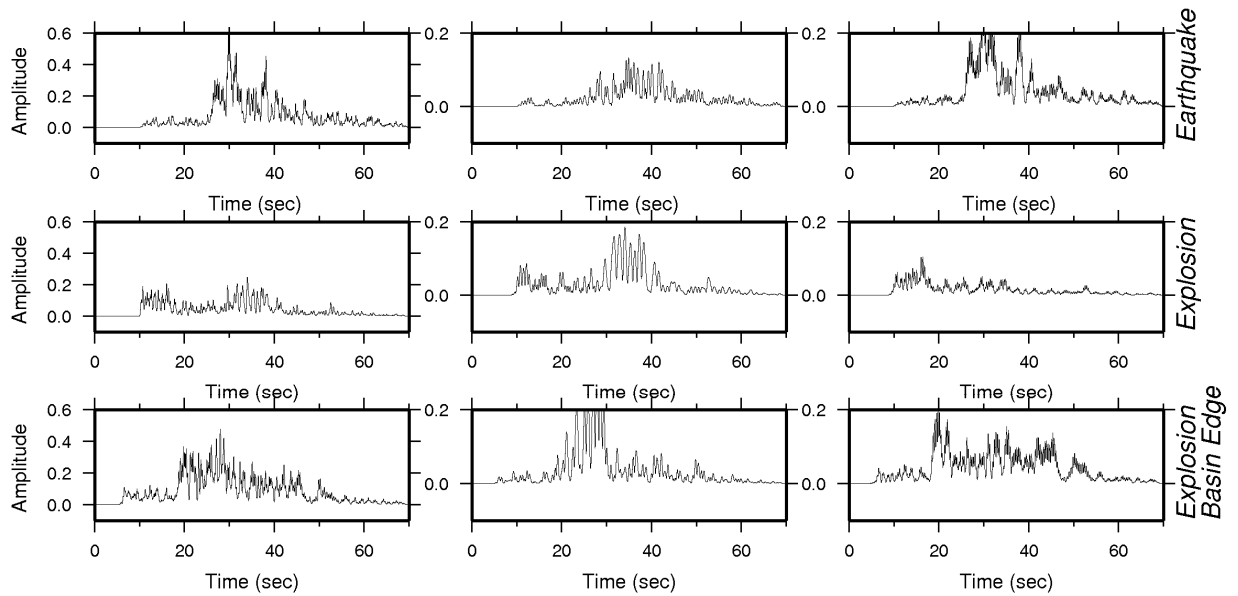
S#16 Rock Site
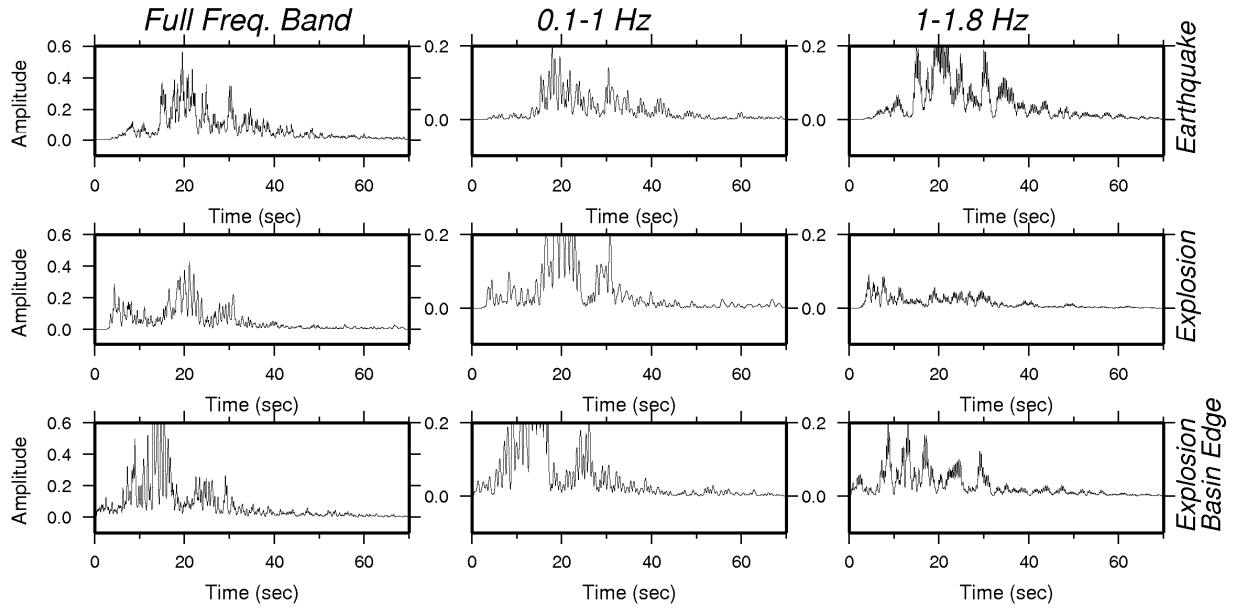
S#26 Basin Site

Figure 17. Comparison of smoothed envelopes of the vertical component of velocity calculated at station S16 (left panels) and station S26 (right panels) between an earthquake at a depth of 7 km, explosion located outside the basin at depth of 400m (RE), and explosion located within the basin at a depth of 400 m (BE).
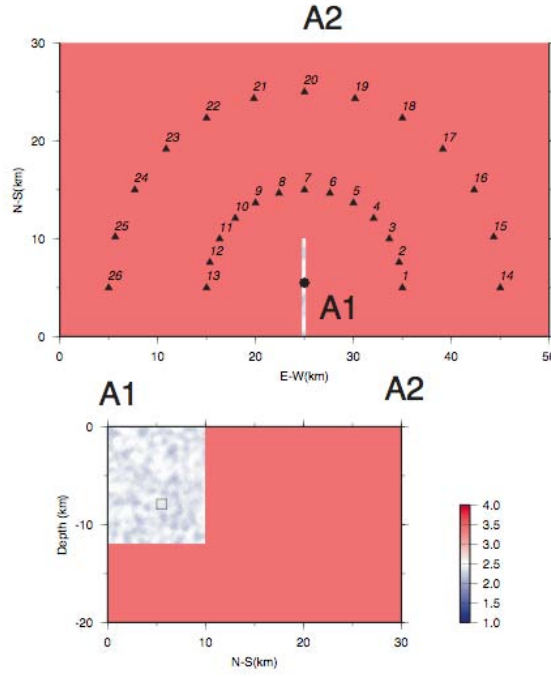
Figure 18. Top panel: Surface view of a vertical fault zone and station locations Bottom panel: Cross-section of the 3D model across the fault zone along line A1-A2. The velocity heterogeneity in the fault zone is modeled by perturbing the shear modulus by +/- 10% with a correlation length of 1 km. Small rectangle shows the location of a 1kmx1km fault used in the simulations of rupture directivity.
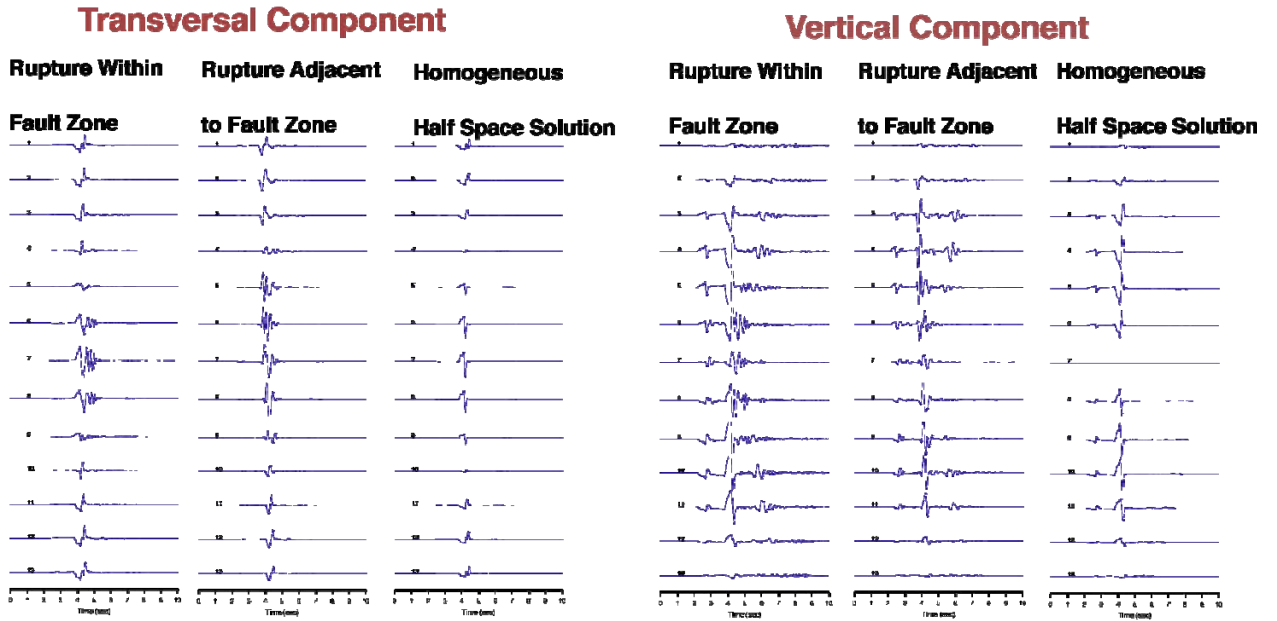
Figure 19. Tangential component (left panels) and vertical component (right panels) of finite-difference synthetic velocity seismograms band-pass filtered at 0.1-7Hz. The station number is indicated on the left of each trace. The small fault ruptures toward north. We considered three scenarios; fault located in the fault zone, fault located next to the fault zone and a reference scenario for a fault embedded in a homogeneous half space.

38
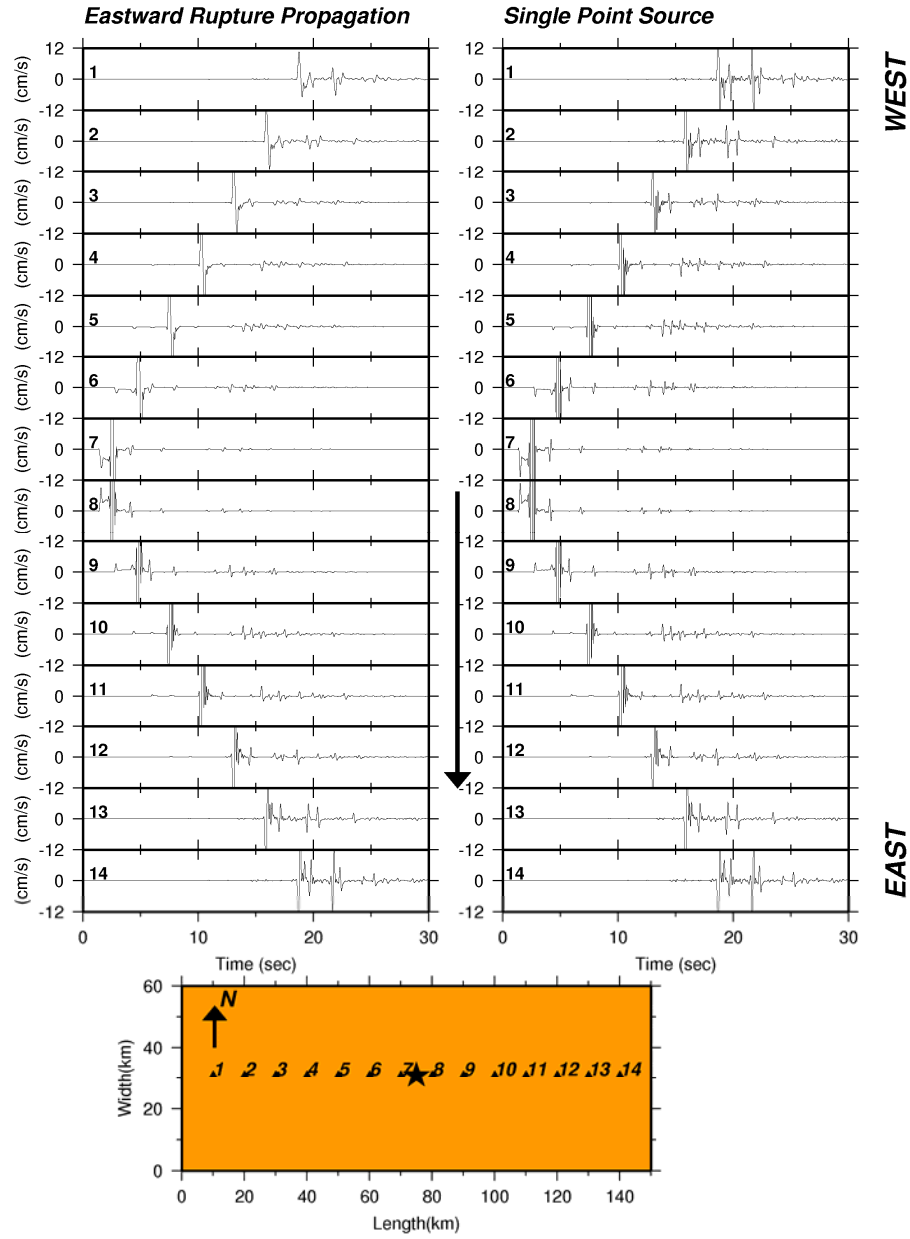
Figure 20a. Rupture directivity at a linear array of stations simulated using 4 double-couple point sources with pure strike-slip mechanism, activated at equal time intervals to simulate unilateral rupture propagation. We used a reference 1D layered model to simulate velocity seismograms up to 6.5Hz.
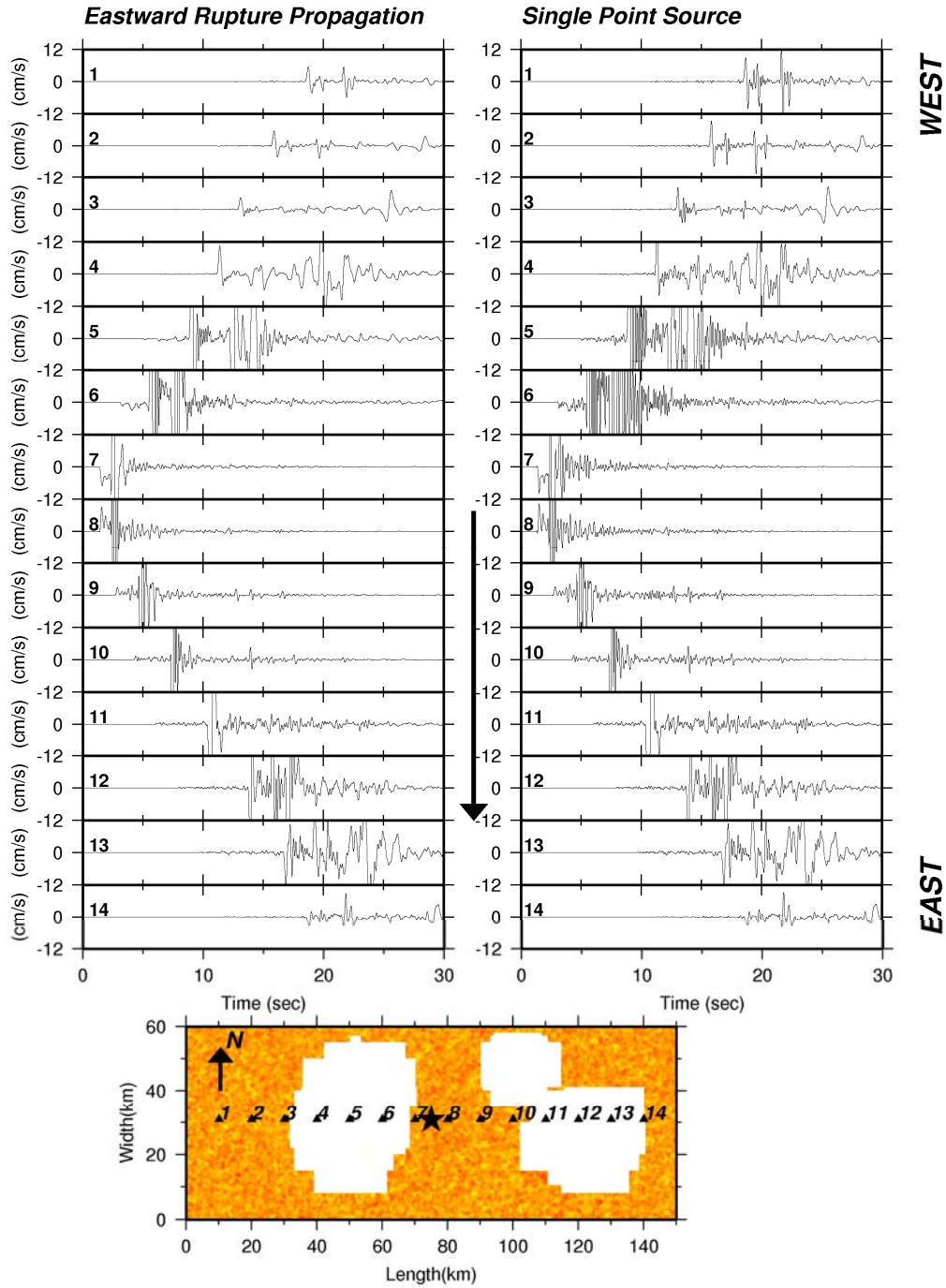
Figure 20b. Same as Figure 20a but for a 3D velocity model with velocity perturbations .
The 3D velocity model used in the finite-difference simulations is the horizontally
layered model with shallow basins, and random perturbations in the upper 6 km.
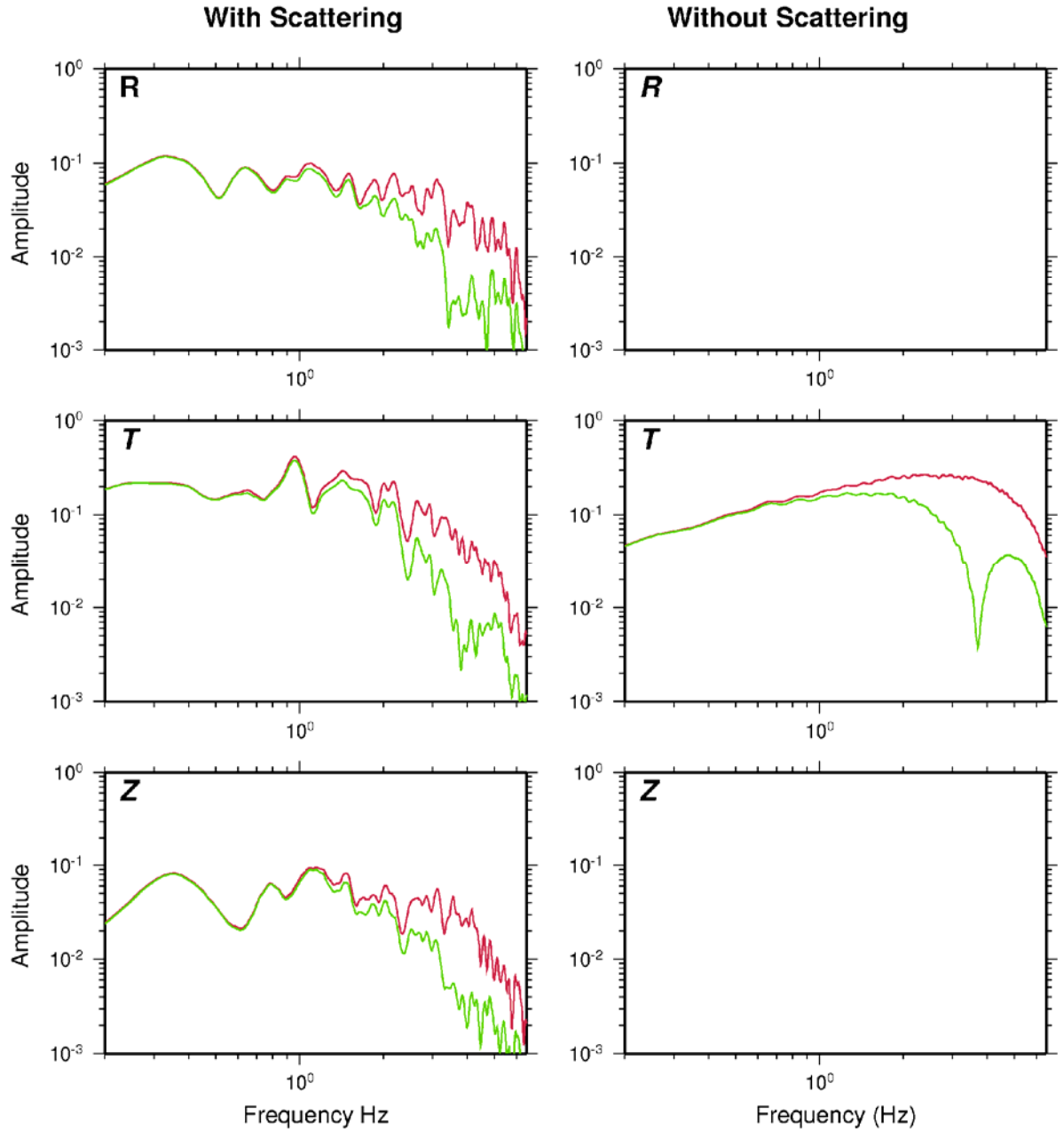
Figure 21. Comparison of amplitude Fourier spectra of velocity calculated at station 12 which recorded the forward rupture directivity (red trace) and station 4 which recorded the backward rupture directivity (green trace). Left panels correspond to the 3D model with scattering, and right panels correspond to 1D model.
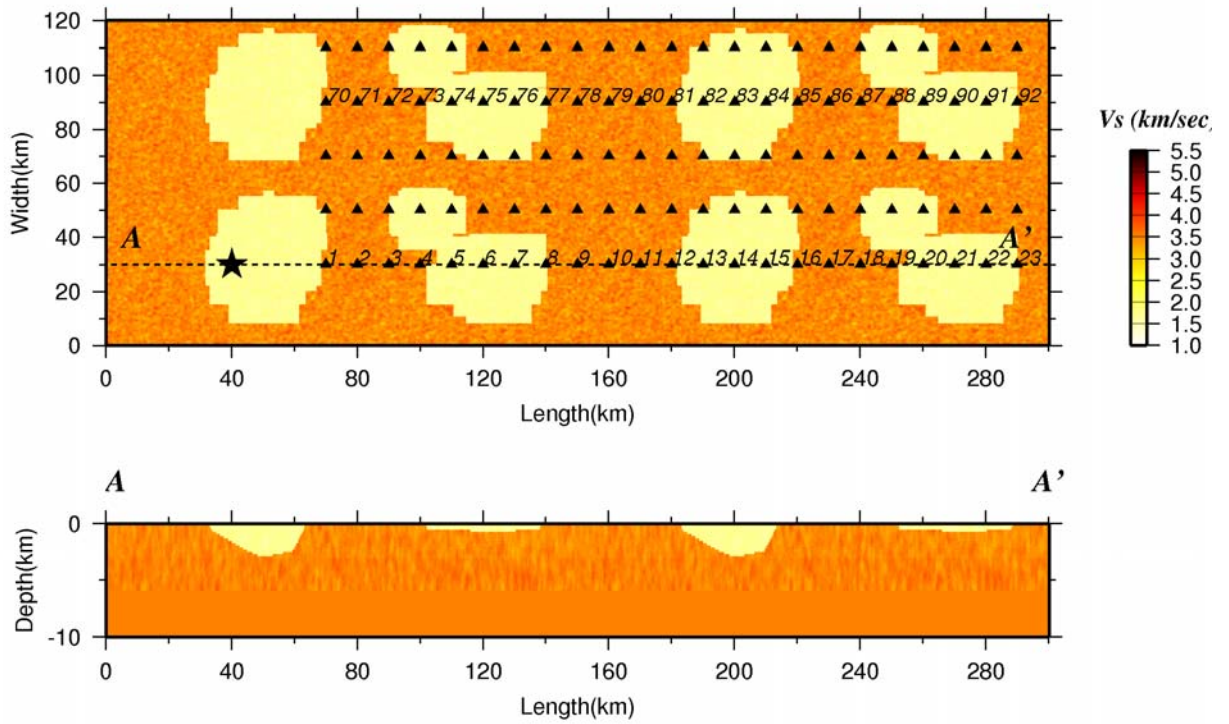
Figure 22. 3D regional velocity model used in modeling wave propagation scattering using flat free surface. Top Panel: Free surface of the 3D velocity model. Yellow colored area are shallow basins. Star indicates the hypocenter location of the source and triangles show the stations location. Bottom Panel: Top 10 km of a vertical cross section of the 3D velocity model along A-A' line
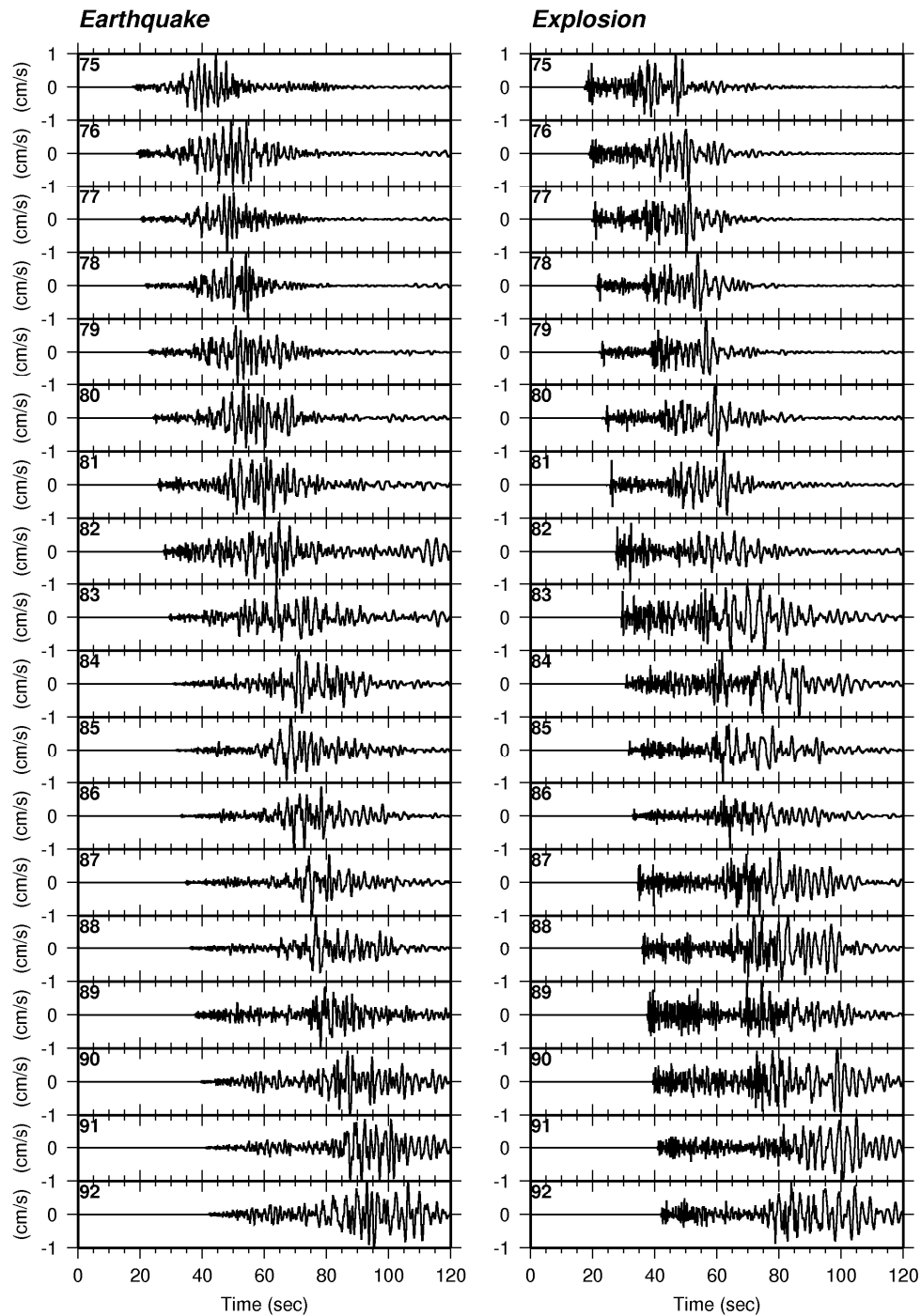
Figure 23a. Vertical component of synthetic velocity for a strike-slip earthquake with the source depth of 2km (left panel) and an isotropic explosion source at a depth of 0.5 km (right panel) band-pass filtered at 0.1-3.5 Hz. All synthetics are individually scaled by their maximum amplitude.
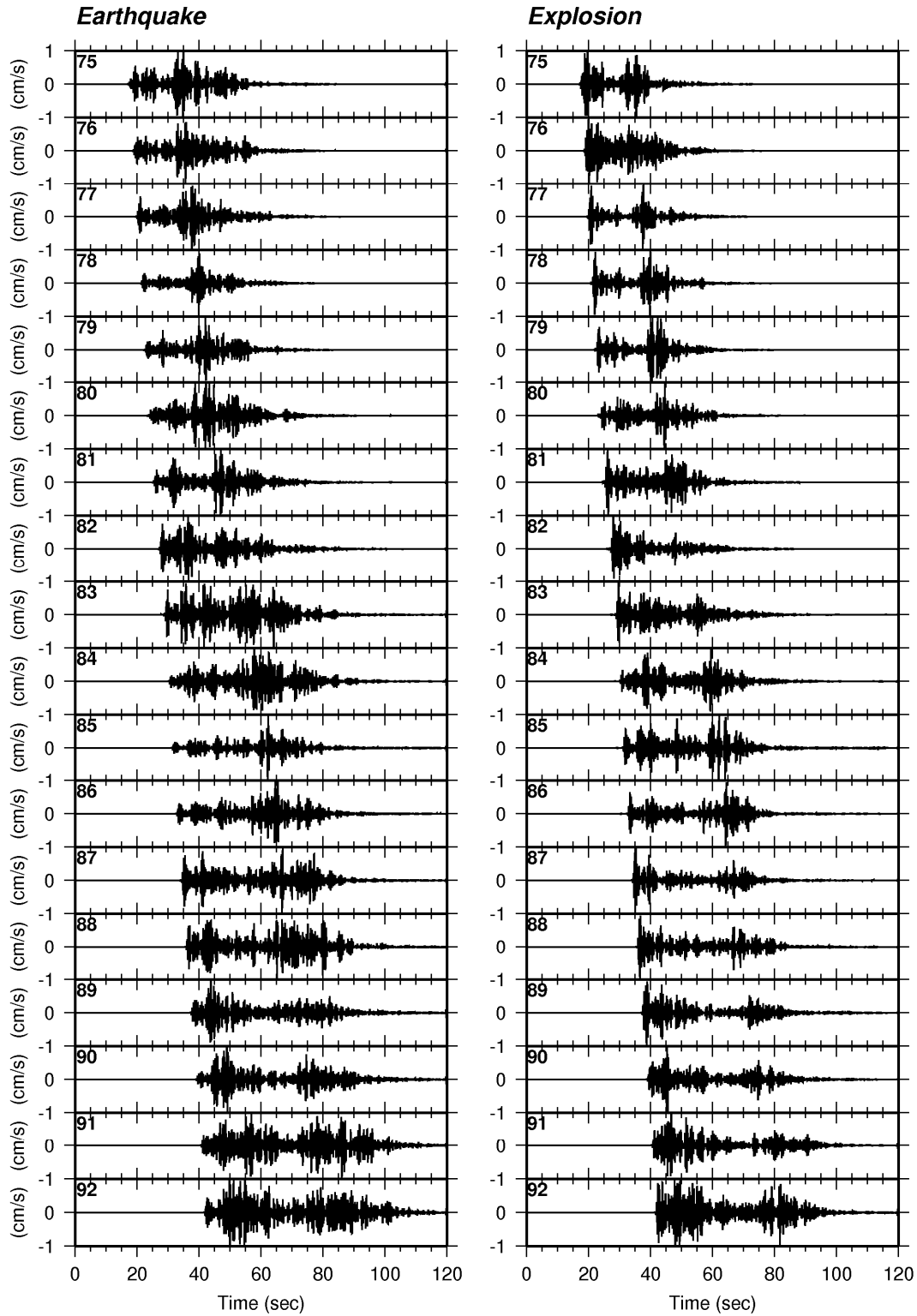
Figure 23b. Same as Figure23a but band-pass filtered at 2.0-3.5 Hz

44
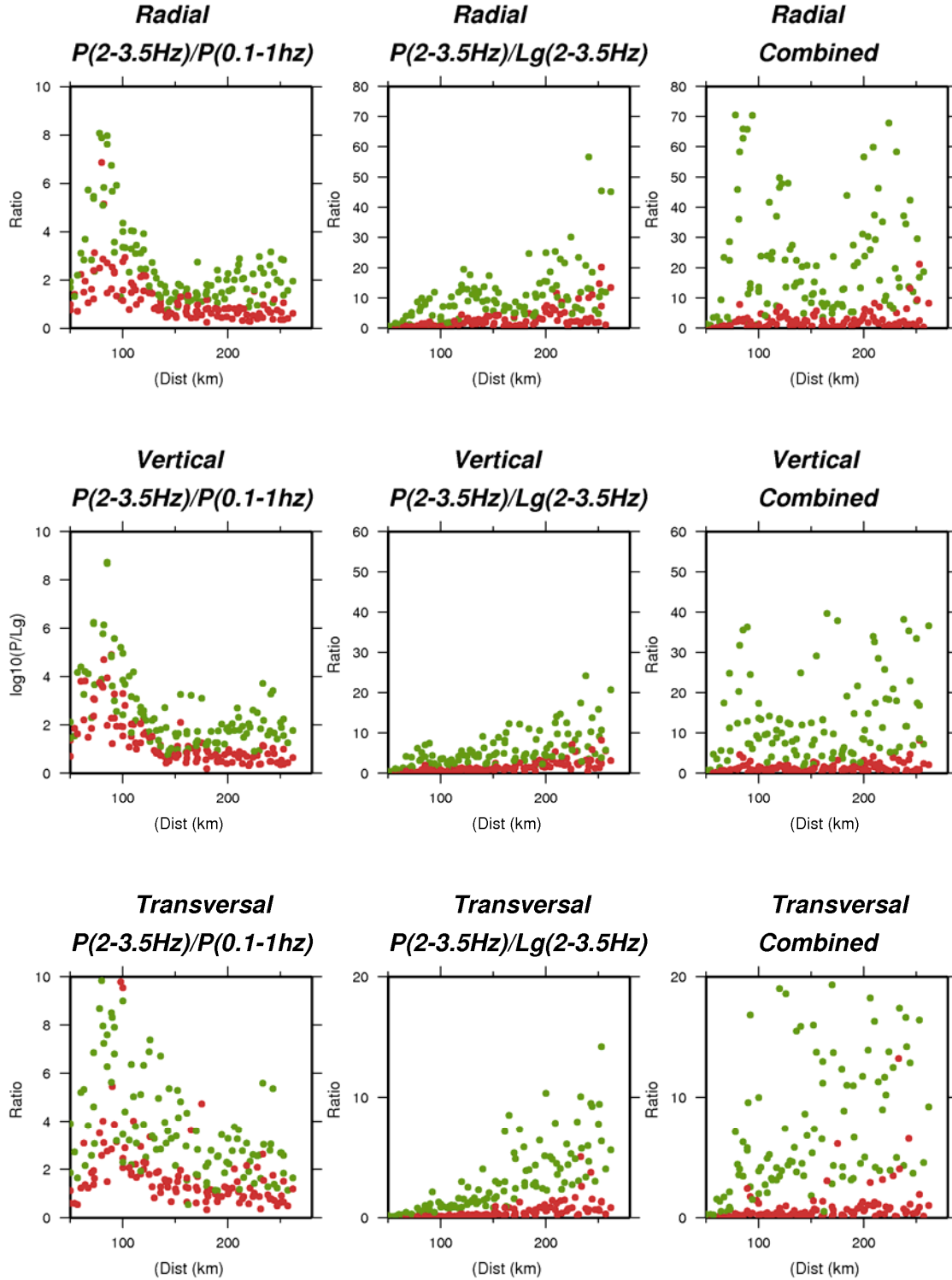
Figure 24. Simulated P(2-3.5Hz)/P(0.1-1.0Hz) ratios (left panels) P(2-3.5Hz)/Lg(2-3.5Hz) ratios (middle panels) and P(2-3.5Hz)/P(0.1-1.0Hz) *P(2-3.5Hz)/Lg(2-3.5Hz) ratios (right panels) for an explosion (green dots) and a shallow earthquake (red dots) for radial, transverse, and vertical component of waveforms. The synthetic are calculated with a 3D multilayer velocity model with random perturbations in the top 6 km. the velocity model is shown in Figure22.

REFERENCES

Bullitt, J.T. and N.M. Toksoz, 1985: Three-dimensional ultrasonic modeling of Rayleigh wave propagation. *Bull. Seism. Soc. Am.*, **75**, 1087-1104.

Campillo, M., and A. Paul, 1992: Influence of lower crustal structure on early coda of regional seismograms. *J. Geophys. Res.*, **97(B3)**, 3405-3416.

Dainty, A. 1996: The influence of seismic scattering on monitoring. *Monitoring a Comprehensive Test Ban Treaty. E.S. Husebye and A.M. Dainty (Editors)*,663-688.

Day, S.M. and C.R. Bradley, 2001: Memory-efficient simulation of anelastic wave propagation. *Bull. Seism. Soc. Am.*, **91(3)**, 520-531.

Day, S.M. and K.L. McLaughlin, 1991: Seismic source representations for spall. *Bull. Seism. Soc. Am.* **81**,191-201.

Frankel, A. and R.W. Clayton, 1986: Finite difference simulations of seismic scattering: implications for the propagation of short-period seismic waves in the crust and models of crustal heterogeneity. *J. Geophys. Res.*, **91(B6)**, 6465-6489.

Frankel, A. and J. Vidale, 1992: A three-dimensional simulation of seismic waves in the Santa Clara Valley, California, from a Loma Prieta aftershock. *Bull. Seism. Soc. Am.* **82,** 2045-2074.

Graves, R.W., and S. Day, 2003: Stability and accuracy analysis of coarse-grain viscoelastic simulations. *Bull. Seism. Soc. Am.*, **93(1)**, 283-300, doi: 10.1785/0120020094

Graves, R., and A. Pitarka, 2004: Broadband time history simulation using a hybrid approach. *Proceeding 13th World Conference on Earthquake Engineering, Vancouver, B. C., Canada, Paper #1098.*

Graves, R.W., A. Pitarka, and P.G. Somerville, 1998: Ground motion amplification in the Santa Monica area: effects of shallow basin edge structure. *Bull. Seism. Soc. Am.*, **88**, 881-897.

Gupta, I.N. and K.L. McLaughlin, 1989**:** Strain and frequency-dependent attenuation estimates in salt based on SALMON and STERLING near-field recordings. *Bull. Seism. Soc. Am.*, **79(4)**, 1111-1121.

He, Y., X.-B. Xie, and T. Lay, 2008: Explosion-source energy Partitioning and *Lg*-Wave excitation: contributions of free-surface scattering. *Bull. Seism. Soc. Am.*, **98(2)**, 778-792.

Jih, R.S. 1994: Statistical characterization of rugged propagation paths with application to Rg scattering study. *Technical Rep. Phillips Laboratory, Kirtland, AFB, NM*

Kanamori, H. and L. Rivera, 2004: Static and dynamic scaling relations for earthquakes and their implications for rupture speed and stress drop. *Bull. Seism. Soc. Am.*, **94(1)**, 314-319, doi: 10.1785/0120030159

Kennedy, D. 1982: Mighty Epic / Diablo Hawk brock motion program, from The Physics of Nonisotropic Source Effects from Underground Explosions, *Report from Structural Mechanics Associates, Newport, CA*

Kim, W. and P.G. Richards, 2007: North Korean Nuclear Test: Seismic Discrimination at Low Yield, *Transactions American Geophysical Union*, **88(14)**, 158-161.

Lay, T. and T. Zhang, 1992: Near-source contributions to teleseismic *P* waves and *P*-wave coda for underground explosions. *Bull. Seism. Soc. Am.*, **82(1)**, 383-405.

Mayeda, K., L. Malagnini, W.S. Phillips, W. Walter, D. Dreger, and P. Morasca, 2005: 2-D path corrections for local and regional coda waves: a test of transport ability. *Proceedings of the 27-th Seismic Research review: Ground –Motion Based Nuclear Explosion Monitoring Technologies*, *Vol. I NNSA*, 587-596.

McLaughlin, K.L. 1986: Network magnitude variation and magnitude bias. *Bull. Seism. Soc. Am.*, **76**, 1813-1816.

McLaughlin, K.L., L.M. Anderson, and A.C. Lees, 1986: Effects of local geologic structure for Yucca Flats, NTS, explosion waveforms: 2-dimensional linear finite difference simulations, *Tech. Report AFGL-TR-86-0220, Geophysics Lab, Hanscom AFB, MA*

McLaughlin, K.L., J.L. Stevens, T.G. Barker, S.M. Day, and B. Skoller, 1993: 2D and 3D numerical modeling of seismic waves from explosion sources. *Computers in Physics*.

Myers, S., J. Wagner, S. Larsen, A. Rodger, K. Mayeda, K. Smith, and W. Walter, 2003: Simulation of regional explosion S-phases (SiRES) Project. *Proceedings of the 25th SRR – Nuclear Explosion Monitoring, Building Knowledge Base, Vol. I NNSA,* 117-124, Tucson, Arizona.

Myers, S.C., J. Wagoner, S. Larsen, L. Preston, and K. Smith, 2005: The effect of topography and near-source geologic heterogeneity on the generation of short-period explosion S waves. *Abstract, SSA Annual Meeting*, Lake Tahoe, 223p.

Ni, J. and Barazangi, M., 1983: High frequency seismic wave propagation beneath the Indian shield, Himalayan Arc, Tibetan Plateau, and surrounding regions: high uppermost mantle velocities and efficient Sn propagation beneath Tibet. *Geophys. Jour. Roy. Astron. Soc.*, **72**, 655-689.

Patton, H.J. 2007: Next Generation Explosion Source Models. *Abstract, SSA Annual Meeting,* Waikoloa, HI.

Patton, H.J, and S.R. Taylor, 1995: Analysis of *Lg* spectral ratios from NTS explosions: Implications for the source mechanisms of spall and generation of Lg waves. *Bull. Seism. Soc. Am.*, 85, 220-236.

Phillips, W.S., H.E. Hartse, S.R. Taylor and G.E. Randall, 2000: 1 Hz Lg Q tomography in central Asia. *Geophys. Res. Lett.*, **27**, 3425-3428.

Phillips, W.S., H.J. Patton, H.E. Hartse, and K.M. Mayeda, 2001: Regional coda magnitude in central Asia and mb(Lg) transportability. *23rd SRR: Worldwide Monitoring of Nuclear explosion, Vol. I NNSA*, 580-589, Jackson Hole, Wyoming.

Pitarka, A. 1999: 3D elastic finite-difference modeling of seismic motion using staggered grid with nonuniform spacing. *Bull. Seism. Soc. Am.*, **89**, 54-68.

Pitarka, A. and L. Dalguer, 2003: Estimation of dynamic stress parameters of the 1992 Landers earthquake. *Abstract, AGU Fall Meeting,* San Francisco, CA.

Pitarka, A and K. Irikura, 1996: Modeling 3D surface topography by finite-difference method: Kobe-JMA station site, Japan case study. *Geophys. Res. Letters*, Vol. 23, **20**, 2729-2732.

Pitarka, A., K. Irikura, T. Iwata, and H. Sekiguchi, 1998: Three-dimensional simulation for the near-fault ground motion for the 1995 Hyogo-Ken Nanbu (Kobe), Japan earthquake. *Bull. Seism. Soc. Am.*, **88**, 428-440.

Rodgers, A. and J. Tromp, 2005: Modeling nuclear explosions and earthquakes using spectral element method and high-performance computing, abstract. Annual SSA meeting at Lake Tahoe, 223p.

Ruzaikian, A.I., Nersesov, I.L. Khalturin, V.I., and Molnar, P., 1977: Propagation of Lg and lateral variation in crustal structure. Asia. *Jour. Geophys. Res*., **82**, 307-316.

Saikia, C.K. 1994: Modified frequency-wave-number algorithm for regional seismograms using Filon's quadrature-modeling of L(g) waves in eastern North America. *Geophys. J. Int.,* **118***,* 142-158.

Saikia, C.K. 1992: Numerical study of quarry generated *Rg* as a discriminant for earthquakes and explosions: modeling of *Rg* in southwestern New England. *J. Geophys. Res.*, **97(B7)**, 11,057–11,072.

Saikia, C.K., D.V. Helmberger, R.J. Stead and B.B. Woods, 2001: Effects of source RDP models and near-source propagation: implication for seismic yield estimation, *Pure and Applied Geophys*., **158**, 2173-2216.

Stead, R. J. 1989: Finite differences and a coupled analytical technique with applications to explosions and earthquakes. Ph.D. Dissertation, California Institute of Technology, Pasadena, CA, p337.

Stead, R. and D. Helmberger, 1988: Numerical-analytical interfacing in two-dimensions with applications to modeling NTS seismograms. *Pageoph,* **128**, 159-174.

Stevens, J.L., G.E. Baker, H, Xu, T. Bennet, N. River, S.M. Day. 2003: The physical basis of Lg generation by explosion sources. *Proceedings of the 25th SRR – Nuclear Explosion Monitoring, Building Knowledge Base, Vol. I NNSA*, 456-465, Tucson, Arizona.

Stevens, J.L., K.L. McLaughlin, B. Shkoller, and S.M. Day, 1993: 2D axisymetric calculations of surface waves generated by ab explosion in an island, mountain, and sedimentary basin. *Geophys. J. Int*., **114**, 548-560.

Takenaka, H., B.L. Kennett, and H. Fujiwara, 1996: Effect of 2-D topography and 3-D seismic wavefield using a 2.5-D discrete wavenumber-boundary integral equation method. *Geophys. J. Int*., **124(3)**, 741-755.

Tan, Y. and D.V. Helmberger, 2009: Rupture directivity of the Big Bear earthquake sequence. *Bull. Seism. Soc. Am*., submitted.

Tan, Y., L. Zhu, D.V. Helmberger, and C.K. Saikia, 2006: Locating and modeling regional earthquakes with two stations. *J. Geophys. Res*., 111, B01306, doi:10.1029/2005JB003775.

Toksoz, M.N., S. Chi, Y. Zhang, E. Sze, and R. Lu, 2005: Characterization of an explosion source in complex medium by modeling and wavelet domain inversion. *Proceedings of the 27th Seismic Research review: Ground –Motion Based Nuclear Explosion Monitoring Technologies,* 683-692*.*

Walter, W.R., E. Matzel, M.E. Pasyanos, D.B. Harris, R. Gok, and S.R. Ford, 2007: Empirical observations of earthquake-explosion discrimination using P/S ratios and implications for the sources of explosions S-waves. *Proceedings of the 29th Monitoring Research Review: Ground-Based Nuclear Explosion Monitoring Technologies, Vol. 3 NNSA*, 684-393, Denver, Colorado

Wu, Ru-Shan, S. Jin, and Xiao-Bi Xie, 2000: Seismic wave propagation and scattering in heterogeneous crustal waveguides using screen propagators: I SH-waves. *Bull. Seism. Soc. Am.*, **90**, 401-413.

Xie, X., T. Lay, and R. Wu, 2005: Near-source energy partitioning for regional waves in 2D and 3D models, contributions of S*-to-Lg and P-to-Lg scattering. *Proceedings of the 27th Seismic Research Review: Ground-Motion Based Nuclear Explosion Monitoring Technologies*, *Vol. I NNSA*, 249-258.

Zhang, T. and T. Lay, 1994: Analyses of short-period regional phase path effects associated with topography in Eurasia. *Bull. Seism. Soc. Am.*, **84**, 119-132.

List of Acronyms

3D-FDM	Three-Dimensional Finite-Difference Methods
AFRL	Air Force Research Laboratory
BEM	Boundary Element Method
CAP	Cut and Paste
CLVD	Compensated Linear Vector Dipole
FSU	Former Soviet Union
NTS	Nevada Test Site
RSTF	Relative Source Time Functions
STS	Semipalatinsk Test Site